ATLAS NOTE

ATLAS-CONF-2017-060

8th July 2017

Search for dark matter and other new phenomena in events with an energetic jet and large missing transverse momentum using the ATLAS detector

The ATLAS Collaboration

Abstract

Results of a search for new phenomena in final states with an energetic jet and large missing transverse momentum are reported. The search uses proton–proton collision data corresponding to an integrated luminosity of 36.1 fb^{-1} at a centre-of-mass energy of 13 TeV collected in 2015 and 2016 with the ATLAS detector at the Large Hadron Collider. Events are required to have at least one jet with a transverse momentum above 250 GeV and no leptons. Several signal regions are considered with increasing requirements on the missing transverse momentum from $E_{\mathrm{T}}^{\mathrm{miss}} > 250$ GeV. Good agreement is observed between the number of events in data and Standard Model predictions. The results are translated into exclusion limits in models with pair-produced weakly interacting dark-matter candidates, large extra spatial dimensions, and supersymmetric particles in several compressed scenarios.

1 Introduction

This note presents the results of a search for events containing an energetic jet and large missing transverse momentum $\vec{p}_{\mathrm{T}}^{\mathrm{miss}}$ (with magnitude $E_{\mathrm{T}}^{\mathrm{miss}}$) in a data sample corresponding to a total integrated luminosity of 36.1 fb^{-1}. The data were collected by the ATLAS Collaboration at the Large Hadron Collider (LHC) from proton–proton collisions at a centre-of-mass energy ($\sqrt{s}$) of 13 TeV. The final-state monojet signature of at least one energetic jet, $E_{\mathrm{T}}^{\mathrm{miss}} > 250$ GeV, and no leptons constitutes a distinctive signature for new physics beyond the Standard Model (SM) at colliders. The monojet signature has been extensively studied at the LHC in the context of searches for large extra spatial dimensions (LED), supersymmetry (SUSY), and weakly interacting massive particles (WIMPs) as candidates for dark matter (DM) [1, 2]. The results of the analysis are therefore interpreted in terms of each of these models, which are described in the following paragraphs.

A range of astrophysical measurements, such as the rotational speed of stars in galaxies and gravitational lensing, point to the existence of a non-baryonic form of matter [3–5]. The existence of a new, weakly interacting massive particle (WIMP) is often hypothesized [6], as it leads to the correct relic density for non-relativistic matter in the early universe [7] as measured by the Planck [8] and WMAP [9] satellites, if the mass is between a few GeV and one TeV and if it has electroweak-scale interaction cross sections. WIMPs may be pair-produced at the LHC and when accompanied by a jet of particles, for example from initial-state radiation (ISR), these events produce the signature of a jet and missing transverse momentum.

As with the initial results obtained in this search channel at $\sqrt{s} = 13$ TeV [1], simplified models are used to interpret the results, providing a framework to characterise the new particles acting as mediators of the interaction between the SM and the dark sector [10–12]. The results from simplified models involving s-channel Feynman diagrams such as the one shown in Figure 1 (left) are comparable to those previously obtained [13] by using an effective-field-theory approach [14] when the mediator mass considered is above 10 TeV [15].

Results are presented for a DM model where Dirac fermion WIMPs (χ) are pair-produced from quarks via s-channel exchange of a spin-1 mediator particle (Z_A) with axial-vector couplings. This leptophobic Z'-like model is defined by four free parameters: the WIMP mass (m_χ), the mediator mass (m_{Z_A}), the flavour-universal coupling to quarks (g_q), and the coupling of the mediator to WIMPs (g_χ). Couplings to other SM particles are not considered. A minimal mediator width is defined by [12]

$$\Gamma(m_{Z_A})_{\mathrm{min}} = \frac{g_\chi^2 m_{Z_A}}{12\pi}\beta_\chi^3\theta(m_{Z_A} - 2m_\chi) + \sum_q \frac{3g_q^2 m_{Z_A}}{12\pi}\beta_q^3\theta(m_{Z_A} - 2m_q)\,, \tag{1}$$

where $\theta(x)$ denotes the Heaviside step function and $\beta_f = \sqrt{1 - \frac{4m_f^2}{m_{Z_A}^2}}$ is the velocity of the Dirac WIMP fermion f (either χ or q) with mass m_f in the mediator rest frame. The quark sum runs over all flavours. The monojet signature in this model emerges from initial-state radiation of a gluon as shown in Figure 1 (left). Similarly, a simplified model with a spin-0 pseudo-scalar mediator in the s-channel is considered.

Supersymmetry is a theory for physics beyond the SM which naturally solves the hierarchy problem and provides candidates for dark matter [16–24]. SUSY introduces a new supersymmetric partner (sparticle) for each particle in the SM. Specifically, a new scalar field is associated with each left- or right-handed quark state. Two squark mass eigenstates $\tilde{q}_1$ and $\tilde{q}_2$ result from the mixing of the scalar fields for a particular flavour. Naturalness arguments suggest that the third generation squarks should be light, with

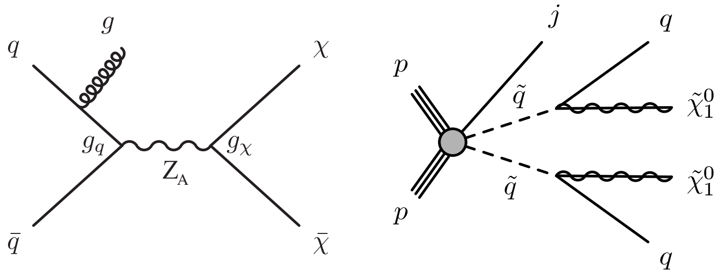

Figure 1: Left: Diagram for the pair-production of weakly interacting massive particles χ, with a leptophobic Z'-like mediator Z_A with axial-vector couplings exchanged in the s-channel. Right: A generic diagram for the pair-production of squarks with the decay mode $\tilde{q} \rightarrow q + \tilde{\chi}_1^0$. The presence of a gluon from initial-state radiation resulting in a jet is indicated for illustration purposes.

masses below about 1 TeV [25]. In addition, many SUSY scenarios have a significant mass difference between the two eigenstates in the bottom-squark (sbottom) and top-squark (stop) sectors, which leads to light sbottom $\tilde{b}_1$ and stop $\tilde{t}_1$ masses. For supersymmetric extensions of the SM that assume R-parity conservation [26–30], sparticles are produced in pairs and the lightest supersymmetric particle (LSP) is stable. The LSP is assumed to be the lightest neutralino $\tilde{\chi}_1^0$ and R-parity conserved.

The results are interpreted in terms of searches for squark production using simplified models in scenarios for which the mass difference $\Delta m \equiv m_{\tilde{q}} - m_{\tilde{\chi}_1^0}$ is small (compressed). Four such scenarios with compressed mass spectra are considered: stop pair production, where the stop decays to a charm quark and the LSP ($\tilde{t}_1 \rightarrow c + \tilde{\chi}_1^0$), stop pair production in the four-body decay mode $\tilde{t}_1 \rightarrow b + f f' + \tilde{\chi}_1^0$, sbottom pair production with $\tilde{b}_1 \rightarrow b + \tilde{\chi}_1^0$, and squark pair production with $\tilde{q} \rightarrow q + \tilde{\chi}_1^0$ ($q = u, d, c, s$). For relatively small Δm ($\lesssim$ 25 GeV), both the transverse momenta of the quark jets and the $E_{\mathrm{T}}^{\mathrm{miss}}$ in the final state are small, making it difficult to fully reconstruct the signal given the kinematic thresholds for reconstruction. The presence of jets from ISR is thus used to identify signal events (see Figure 1 (right)). In this case, the squark-pair system is boosted, leading to larger $E_{\mathrm{T}}^{\mathrm{miss}}$.

The final model considered is that of extra spatial dimensions, the existence of which has been postulated to explain the large difference between the electroweak unification scale at $O(10^2)$ GeV and the Planck scale M_{Pl} at $O(10^{19})$ GeV. In the Arkani-Hamed, Dimopoulos, and Dvali (ADD) model for LED [31], the presence of n extra spatial dimensions of size R leads to a fundamental Planck scale in $4 + n$ dimensions given by ${M_{\mathrm{Pl}}}^2 \sim {M_D}^{2+n} R^n$, where M_D is the fundamental scale of the $4{+}n$-dimensional theory. Motivation for the theory comes from the possibility to make M_D of order 1 TeV, a scale accessible at the LHC. In this model, SM particles and gauge interactions are confined to the usual 3+1 space-time dimensions, whereas gravity is free to propagate through the entire multidimensional space, which effectively dilutes its perceived strength. The extra spatial dimensions are compactified, resulting in a Kaluza-Klein tower of massive graviton modes. If produced in high-energy proton–proton collisions, a graviton escaping into the extra dimensions can be inferred from $E_{\mathrm{T}}^{\mathrm{miss}}$, and can lead to a monojet event signature.

The note is organized as follows. The ATLAS detector is described in the next section. Section 3 provides details of the Monte Carlo simulations used in the analysis for background and signal processes. Section 4 discusses the reconstruction and identification of jets, leptons, and missing transverse momentum, while Section 5 describes the event selection. The estimation of background contributions and the study of systematic uncertainties are discussed in Sections 6 and 7. The results are presented in Section 8 and are interpreted in terms of limits in models for WIMP pair production, ADD, and SUSY in compressed scenarios. Finally, Section 9 is devoted to the conclusions.

2 Experimental setup

The ATLAS detector [32] covers almost the whole solid angle[1] around the collision point with layers of tracking detectors, calorimeters, and muon chambers. The ATLAS inner detector covers the pseudorapidity range $|\eta| < 2.5$. It consists of a silicon pixel detector, a silicon microstrip detector, and a straw tube tracker that also measures transition radiation for particle identification, all immersed in a 2 T axial magnetic field produced by a solenoid. During the first LHC long shutdown, a new tracking layer, known as the Insertable B-Layer [33], was added at a radius of 33 mm.

High-granularity lead/liquid-argon (LAr) electromagnetic sampling calorimeters cover the pseudorapidity range $|\eta| < 3.2$. The hadronic calorimetry in the range $|\eta| < 1.7$ is provided by a steel/scintillator-tile calorimeter, consisting of a large barrel and two smaller extended barrel cylinders, one on either side of the central barrel. In the endcaps ($|\eta| > 1.5$), copper/LAr and tungsten/LAr hadronic calorimeters match the outer $|\eta|$ limits of the endcap electromagnetic calorimeters. The LAr forward calorimeters provide both the electromagnetic and hadronic energy measurements, and extend the coverage to $|\eta| < 4.9$.

The muon spectrometer measures the deflection of muons in the magnetic field provided by large superconducting air-core toroid magnets in the pseudorapidity range $|\eta| < 2.7$, instrumented with separate trigger and high-precision tracking chambers. Over most of the η range, a measurement of the track coordinates in the bending direction of the magnetic field is provided by monitored drift tubes. Cathode strip chambers with higher granularity are used in the innermost plane over $2.0 < |\eta| < 2.7$. The muon fast trigger detectors cover the pseudorapidity range $|\eta| < 2.4$ and provide a measurement of the coordinate in the non-bending plane.

The data were collected using an online two-level trigger system [34] that selects events of interest and reduces the event rate from 33 MHz to about 1 kHz for recording and offline processing.

3 Monte Carlo simulation

Monte Carlo (MC) simulated event samples are used to compute detector acceptance and reconstruction efficiencies, determine signal and background contributions, and estimate systematic uncertainties in the final results. Samples are processed with the full ATLAS detector simulation [35] based on GEANT4 [36]. Simulated events are then reconstructed and analysed with the same analysis chain as for the data, using the same trigger and event selection criteria. The effects of multiple proton–proton interactions in the same or neighbouring bunch-crossings (pileup) are taken into account by overlaying simulated minimum-bias events from PYTHIA-8.205 [37] onto the hard-scattering process, distributed in the same frequency as in data.

---

[1] ATLAS uses a right-handed coordinate system with its origin at the nominal interaction point (IP) in the centre of the detector and the z-axis along the beam pipe. The x-axis points from the IP to the centre of the LHC ring, and the y-axis points upward. Cylindrical coordinates (r, ϕ) are used in the transverse plane, ϕ being the azimuthal angle around the z-axis. The pseudorapidity is defined in terms of the polar angle θ as $\eta = -\ln\tan(\theta/2)$.

3.1 Signal simulation

WIMP s-channel signal samples are simulated in Powheg-Box v2 [38–40] (revision 3049) using two implementations of simplified models, introduced in Ref. [41]. The DMV model of WIMP pair production is used for s-channel spin-1 axial-vector mediator exchange at next-to-leading order (NLO), and the DMS_tloop model is used for WIMP pair production with the s-channel spin-0 pseudo-scalar mediator exchange with the full quark-loop calculation at leading order (LO) [42]. Renormalization and factorization scales are set to $H_{\mathrm{T}}/2$ on an event-by-event basis, where $H_{\mathrm{T}} = \sqrt{m_{\chi\chi}^2 + p_{\mathrm{T},j1}^2} + p_{\mathrm{T},j1}$ is defined by the invariant mass of the WIMP pair ($m_{\chi\chi}$) and the transverse momentum of the highest p_{T} jet ($p_{\mathrm{T},j1}$). The mediator propagator is described by a Breit-Wigner distribution. Events are generated using the NNPDF30 [43] parton distribution functions (PDFs) and interfaced to Pythia-8.205 with the A14 set of tuned parameters [44] for parton showering. Couplings of the mediator to WIMP particles and those of the SM quarks are set to $g_\chi = 1$ and $g_q = 1/4$ for the DMV model whereas both couplings are set to one in the case of the DMS_tloop model. A grid of samples is produced for WIMP masses ranging from 1 GeV to 1 TeV and mediator masses between 10 GeV and 10 TeV.

SUSY signals for stop pair production are generated with MG5_aMC@NLO v5.2.2.3 [45] and interfaced to Pythia 8.186 with the A14 tune for modelling of the squark decay, parton showering, hadronization, and underlying event. The PDF used for the generation is NNPDF23LO, and the renormalization and factorization scales are set to the sum of transverse masses of all final-state particles. The matrix-element calculation is performed at tree level, and includes the emission of up to two additional partons. Matching to parton-shower calculations is accomplished by the CKKW-L prescription [46], with a matching scale set to one quarter of the pair-produced superpartner mass. Signal cross sections are calculated at NLO in the strong coupling constant, adding the resummation of soft-gluon emission at next-to-leading-logarithmic (NLO+NLL) accuracy [47–49]. The nominal cross section and its uncertainty are taken from an envelope of cross-section predictions using different PDF sets and factorization and renormalization scales, as described in Ref. [50]. Simulated samples are produced with squark masses in the range between 250 GeV and 700 GeV and Δm varying between 5 GeV and 25 GeV.

Simulated samples for the ADD LED model with different numbers of extra dimensions in the range $n = 2$–6 and M_D in the range 3–5.3 TeV are generated using Pythia-8.205 with NNPDF23LO [51] PDFs. The renormalization scale is set to the geometric mean of the squared transverse masses of the two produced particles, $\sqrt{(p_{\mathrm{T},G}^2 + m_G^2)(p_{\mathrm{T},p}^2 + m_p^2)}$, where m_G and $p_{\mathrm{T},G}$ (m_p and $p_{\mathrm{T},p}$) denote, respectively, the mass and the transverse momentum of the graviton (parton) in the final state. The factorization scale is set to the minimum transverse mass, $\sqrt{m^2 + p_{\mathrm{T}}^2}$, of the graviton and the parton.

3.2 Background simulation

After applying the selection described in Section 5, the primary SM background contributing monojet event signatures is $Z(\rightarrow \nu\bar{\nu})$+jets. There are significant contributions also from W+jets events, primarily from $W(\rightarrow \tau\nu)$+jets. Small contributions are expected from $Z/\gamma^*(\rightarrow \ell^+\ell^-)$+jets ($\ell = e, \mu, \tau$), multijet, $t\bar{t}$, single-top, and diboson (WW, WZ, ZZ) processes. Contributions from top production associated with additional vector bosons ($t\bar{t} + W$, $t\bar{t} + Z$, or $t + Z + q/b$ processes) are negligible and not considered in this analysis.

Events containing W or Z bosons with associated jets are simulated using the Sherpa-2.2.1 [52] generator. Matrix elements (ME) are calculated for up to two partons at next-to-leading order (NLO) and four partons at LO using the Comix [53] and OpenLoops [54] matrix-element generators and merged with the Sherpa parton shower (PS) [55] using the ME+PS@NLO prescription [56]. The CT10 [57] PDF set is used in conjunction with a dedicated parton-shower tuning developed by the authors of Sherpa. The MC predictions are initially normalized to next-to-next-to-leading-order (NNLO) perturbative QCD (pQCD) predictions according to DYNNLO [58, 59] using MSTW2008 90% CL NNLO PDF sets [60].

The W+jets and Z+jets MC predictions are reweighted to account for higher-order QCD and electroweak corrections as described in Ref. [61], where parton-level predictions for W/Z+jet production, including throughout NNLO QCD corrections and NLO electroweak corrections supplemented by Sudakov logarithms at two loops, are provided as a function of the boson-p_{T}, improving the description of the measured Z-boson p_{T} distribution [62]. The predictions are provided separately for the different W+jet and Z+jet processes together with the means for a proper estimation of theoretical uncertainties and their correlations (see Section 7). The reweighting procedure takes into account the difference between the QCD NLO predictions as included already in Sherpa and as provided by the parton-level calculations.

For the generation of $t\bar{t}$ and single top-quarks in the Wt-channel and s-channel, the Powheg-Box v2 [63] generator is used with CT10 PDFs. Electroweak t-channel single top-quark events are generated using the Powheg-Box v1 generator. This generator uses the four-flavour scheme for calculation of NLO matrix elements, with the four-flavour PDF set CT10. The parton shower, fragmentation, and underlying event are simulated using Pythia-8.205 with the A14 set of tuned parameters. The top-quark mass is set to 172.5 GeV. The EvtGen v1.2.0 program [64] is used to model the decays of the bottom and charm hadrons. Alternative samples are generated using MadGraph5_aMC@NLO (v2.2.1) [45] interfaced to Herwig++ (v2.7.1) [65] in order to estimate the effects of the choice of matrix-element event generator and parton-shower algorithm.

Diboson samples (WW, WZ, and ZZ production) are generated using Sherpa-2.2.0 with CT10 PDFs and are normalized to NLO pQCD predictions [66]. Diboson samples are also generated using Powheg [39] interfaced to Pythia-8.186 and using CT10 PDFs for studies of systematic uncertainties.

4 Event reconstruction

Jets are reconstructed from energy deposits in the calorimeters using the anti-k_t jet algorithm [67] with the radius parameter (in y–ϕ space) set to 0.4. The measured jet transverse momentum is corrected for detector effects, including the noncompensating character of the calorimeter, by weighting energy deposits arising from electromagnetic and hadronic showers differently. In addition, jets are corrected for contributions from pileup, as described in Ref. [68]. Jets with $p_{\mathrm{T}} > 20$ GeV and $|\eta| < 2.8$ are considered in the analysis. Track-based variables to suppress pileup jets have been developed, and a combination of two such variables, called the jet-vertex tagger (JVT), is constructed. In order to remove jets originating from pileup collisions, for central jets ($|\eta| < 2.4$) with $p_{\mathrm{T}} < 50$ GeV a significant fraction of the tracks associated with each jet must have an origin compatible with the primary vertex, as defined by the JVT [69].

Jets are identified as b-jets if tagged by a multivariate algorithm which uses information about the impact parameters of inner-detector tracks matched to the jet, the presence of displaced secondary vertices, and the reconstructed flight paths of b- and c-hadrons inside the jet [70, 71]. A 60% efficient b-tagging working point, as determined in a simulated sample of $t\bar{t}$ events, is chosen. This corresponds to a rejection factor of approximately 1500, 35 and 180 for light quark and gluon jets, c-jets, and τ-leptons decaying hadronically, respectively.

The presence of leptons (electrons or muons) in the final state is used in the analysis to define control samples and to reject background contributions in the signal regions (see Sections 5 and 6).

Electrons are found by combining energy deposits in the calorimeter with tracks found in the inner detector, and are initially required to have $p_{\mathrm{T}} > 20$ GeV and $|\eta| < 2.47$, and to satisfy the 'Loose' electron shower shape and track selection criteria described in Refs. [72]. Overlaps between identified electrons and jets with $p_{\mathrm{T}} > 30$ GeV in the final state are resolved. Jets are discarded if they are not b-tagged and their separation $\Delta R = \sqrt{(\Delta\eta)^2 + (\Delta\phi)^2}$ from an identified electron is less than 0.2. Otherwise, the electron is removed as it is likely coming from a semileptonic b-hadron decay. The electrons separated by ΔR between 0.2 and 0.4 from any remaining jet are removed.

Muon candidates are required to have $p_{\mathrm{T}} > 10$ GeV and $|\eta| < 2.5$, and are formed by combining information from the muon spectrometer and inner tracking detectors, as described in Ref. [73]. Jets with $p_{\mathrm{T}} > 30$ GeV and fewer than three tracks with $p_{\mathrm{T}} > 0.5$ GeV associated with them are discarded if their separation ΔR from an identified muon is less than 0.4. The muon is discarded if it is matched to a jet with $p_{\mathrm{T}} > 30$ GeV that has at least three tracks associated with it.

The $E_{\mathrm{T}}^{\mathrm{miss}}$ is reconstructed using all energy deposits in the calorimeter up to pseudorapidity $|\eta| = 4.9$. Clusters associated with either electrons, photons or jets with $p_{\mathrm{T}} > 20$ GeV make use of the corresponding calibrations for these objects. Softer jets and clusters not associated with these objects are calibrated using tracking information [74]. As discussed below, in this analysis the $E_{\mathrm{T}}^{\mathrm{miss}}$ is not corrected for the presence of muons in the final state.

5 Event selection

The data sample considered corresponds to a total integrated luminosity of 36.1 fb^{-1}, and was collected in 2015 and 2016. The uncertainty in the combined 2015+2016 integrated luminosity is 3.2%. It is derived, following a methodology similar to that detailed in Ref. [75], from a preliminary calibration of the luminosity scale using x–y beam-separation scans performed in August 2015 and May 2016. The data were collected using a trigger that selects events with $E_{\mathrm{T}}^{\mathrm{miss}}$ above 90 GeV, as computed by calorimetry information at the final stage of the two-level ATLAS trigger system. After analysis selections, the trigger was measured to be fully efficient for events with $E_{\mathrm{T}}^{\mathrm{miss}} > 250$ GeV, as determined using a data sample with muons in the final state. Events are required to have at least one reconstructed primary vertex consistent with the beamspot envelope and that contains at least two associated tracks of $p_{\mathrm{T}} > 0.4$ GeV. When more than one such vertex is found, the vertex with the largest summed p_{T}^2 of the associated tracks is chosen. Events having identified muons with $p_{\mathrm{T}} > 10$ GeV or electrons with $p_{\mathrm{T}} > 20$ GeV in the final state are vetoed.

Events are selected with $E_{\mathrm{T}}^{\mathrm{miss}} > 250$ GeV, where a leading (highest-p_{T}) jet with $p_{\mathrm{T}} > 250$ GeV and $|\eta| < 2.4$ is required. A maximum of four jets with $p_{\mathrm{T}} > 30$ GeV and $|\eta| < 2.8$ are allowed. Separation in the azimuthal plane of $\Delta\phi(\mathrm{jet}, \vec{p}_{\mathrm{T}}^{\,\mathrm{miss}}) > 0.4$ between the missing transverse momentum direction and each selected jet is required to reduce the multijet background contribution where a large $E_{\mathrm{T}}^{\mathrm{miss}}$ can originate from jet energy mismeasurement.

Jet quality criteria [76] are imposed, which involve selections based on quantities such as the pulse shape of the energy depositions in the cells of the calorimeters, electromagnetic fraction in the calorimeter, calorimeter sampling fraction, and the charged-particle fraction.[2] Loose selection criteria are applied to all jets with $p_{\mathrm{T}} > 30$ GeV and $|\eta| < 2.8$, which removes anomalous energy depositions due to coherent noise and electronic noise bursts in the calorimeter [77]. Events with any jet failing the loose criteria are discarded.

Non-collision backgrounds, for example energy depositions in the calorimeters due to muons of beam-induced or cosmic-ray origin, are suppressed by applying tight selection criteria on the leading jet; the ratio of the jet charged-particle fraction to the calorimeter sampling fraction,[3] $f_{\mathrm{ch}}/f_{\mathrm{max}}$, is required to be larger than 0.1. These requirements have a negligible effect on the signal efficiency.

The analysis uses two sets of signal regions, with inclusive and exclusive $E_{\mathrm{T}}^{\mathrm{miss}}$ selections, where the regions are defined with increasing $E_{\mathrm{T}}^{\mathrm{miss}}$ thresholds from 250 GeV to 1000 GeV (see Table 1). The inclusive selections are used for a model-independent search for new physics, and the exclusive selections are used for the interpretation of the results within different models for new physics.

Table 1: Inclusive (IM1–IM10) and exclusive (EM1–EM10) signal regions with increasing $E_{\mathrm{T}}^{\mathrm{miss}}$ thresholds from 250 GeV to 1000 GeV. In the case of IM10 and EM10, both signal regions contain the same selected events in data. In the case of the IM10, the background predictions are computed considering only data and simulated events with $E_{\mathrm{T}}^{\mathrm{miss}} > 1$ TeV, whereas the EM10 background prediction is obtained from fitting the full $E_{\mathrm{T}}^{\mathrm{miss}}$ shape in data and simulation (see Section 6).

Inclusive (IM)	IM1	IM2	IM3	IM4	IM5	IM6	IM7	IM8	IM9	IM10
$E_{\mathrm{T}}^{\mathrm{miss}}$ (GeV)	>250	>300	>350	>400	>500	>600	>700	>800	>900	>1000
Exclusive (EM)	EM1	EM2	EM3	EM4	EM5	EM6	EM7	EM8	EM9	EM10
$E_{\mathrm{T}}^{\mathrm{miss}}$ (GeV)	250–300	300–350	350–400	400–500	500–600	600–700	700–800	800–900	900–1000	>1000

6 Background estimation

The W+jets, Z+jets, and top-quark related backgrounds are constrained using MC event samples normalized with data in selected control regions. By construction, there is no overlap between events in the signal and the different control regions. The control regions are defined using the same requirements for $E_{\mathrm{T}}^{\mathrm{miss}}$, leading-jet p_{T}, event topologies, and jet vetoes as in the signal regions, such that no extrapolation in $E_{\mathrm{T}}^{\mathrm{miss}}$ or jet p_{T} is needed from control to signal regions. The normalization factors are extracted simultaneously using a global fit that includes systematic uncertainties, to properly take into account correlations.

Different control samples are used to help constrain the yields of the W+jets and Z+jets background processes in the signal regions. This includes $W(\rightarrow \mu\nu)$+jets, $W(\rightarrow e\nu)$+jets, and $Z/\gamma^{*}(\rightarrow \mu^{+}\mu^{-})$+jets control samples, enriched in $W(\rightarrow \mu\nu)$+jets, $W(\rightarrow e\nu)$+jets, and $Z/\gamma^{*}(\rightarrow \mu^{+}\mu^{-})$+jets background processes, respectively. The dominant $Z(\rightarrow \nu\bar{\nu})$+jets and $W(\rightarrow \tau\nu)$+jets background contributions are constrained in the fit by using both W+jets control regions and the $Z/\gamma^{*}(\rightarrow \mu^{+}\mu^{-})$+jets control region. As discussed in

---

[2] The charged-particle fraction is defined as $f_{\mathrm{ch}} = \sum p_{\mathrm{T}}^{\mathrm{track,jet}}/p_{\mathrm{T}}^{\mathrm{jet}}$, where $\sum p_{\mathrm{T}}^{\mathrm{track,jet}}$ is the scalar sum of the transverse momenta of tracks associated with the primary vertex within a cone of radius $\Delta R = 0.4$ around the jet axis, and $p_{\mathrm{T}}^{\mathrm{jet}}$ is the transverse momentum as determined from calorimetric measurements.

[3] f_{max} denotes the maximum fraction of the jet energy collected by a single calorimeter layer.

Section 6.4, this translates into a reduced uncertainty in the estimation of the main irreducible background contribution, due to a partial cancellation of systematic uncertainties and the superior statistical power of the W+jets control sample in data, compared to that of the $Z/\gamma^*(\rightarrow \mu^+\mu^-)$+jets control sample. Finally, a small $Z/\gamma^*(\rightarrow e^+e^-)$+jets and $Z/\gamma^*(\rightarrow \tau^+\tau^-)$+jets background contribution is also constrained via the W+jets and $Z/\gamma^*(\rightarrow \mu^+\mu^-)$+jets control samples[4].

Finally, a top control sample constrains top-quark related background processes. The remaining SM backgrounds from diboson processes are determined using MC simulated samples, while the multijet background contribution is extracted from data. The contributions from non-collision backgrounds are estimated in data using the beam-induced background identification techniques described in Ref. [77].

In the following subsections, details of the definition of the W/Z+jets and top control regions, and of the data-driven determination of the multijet and beam-induced backgrounds are given. This is followed by a description of the background fits.

6.1 Control samples

A $W(\rightarrow \mu\nu)$+jets control sample is selected by requiring a muon consistent with originating from the primary vertex with $p_{\rm T} > 10$ GeV, and transverse mass in the range 30 GeV $< m_{\rm T} <$ 100 GeV. The transverse mass $m_{\rm T} = \sqrt{2p_{\rm T}^{\ell}p_{\rm T}^{\nu}[1-\cos(\phi^{\ell}-\phi^{\nu})]}$ is defined by the lepton and neutrino transverse momenta, where the (x,y) components of the neutrino momentum are taken to be the same as the corresponding $\vec{p}_{\rm T}^{\rm\ miss}$ components. Events with identified electrons in the final state are vetoed. In addition, events with an identified b-jet in the final state are vetoed in order to reduce the contamination from top-quark related processes. Similarly, a $Z/\gamma^*(\rightarrow \mu^+\mu^-)$+jets control sample is selected by requiring the presence of two muons with $p_{\rm T} > 10$ GeV and invariant mass in the range 66 GeV $< m_{\mu\mu} <$ 116 GeV. In the $W(\rightarrow \mu\nu)$+jets and $Z/\gamma^*(\rightarrow \mu^+\mu^-)$+jets control regions, the $E_{\rm T}^{\rm miss}$ is not corrected for the presence of the muons in the final state, motivated by the fact that these control regions are used to estimate the $Z(\rightarrow \nu\bar{\nu})$+jets, $W(\rightarrow \mu\nu)$+jets and $Z/\gamma^*(\rightarrow \mu^+\mu^-)$+jets backgrounds in the signal regions with no identified muons. The $E_{\rm T}^{\rm miss}$-based online trigger used in the analysis does not include muon information in the $E_{\rm T}^{\rm miss}$ calculation. This allows the collection of $W(\rightarrow \mu\nu)$+jets and $Z/\gamma^*(\rightarrow \mu^+\mu^-)$+jets control samples with the same trigger as for the signal regions.

A $W(\rightarrow e\nu)$+jets dominated control sample is collected using online triggers that select events with an electron in the final state. The control sample is defined with an isolated electron candidate with $p_{\rm T} > 30$ GeV, 30 GeV $< m_{\rm T} <$ 100 GeV, and no additional identified leptons in the final state. Electron candidates in the crack region $1.37 < |\eta| < 1.52$ are excluded. The $E_{\rm T}^{\rm miss}$ is corrected by subtracting the contribution from the electron cluster in the calorimeter. In this way, the measured $E_{\rm T}^{\rm miss}$ in the event reflects better the magnitude of the W-boson $p_{\rm T}$ in the final state, which is necessary for a proper implementation of W-boson $p_{\rm T}$ reweighting procedure, as explained in Section 3, that accounts for higher-order QCD and electroweak corrections. In order to suppress backgrounds from multijet processes with jets faking high-$p_{\rm T}$ electrons, the events are required to have $E_{\rm T}^{\rm miss}/\sqrt{H_{\rm T}} > 5$ GeV$^{1/2}$, where in this case $E_{\rm T}^{\rm miss}$ still includes the contribution from the electron energy deposits in the calorimeter and $H_{\rm T}$ denotes the scalar sum of the $p_{\rm T}$ of the identified jets in the final state.

---

[4] The use of an additional $Z/\gamma^*(\rightarrow e^+e^-)$+jets control sample for constraining the $Z/\gamma^*(\rightarrow e^+e^-)$+jets and $Z(\rightarrow \nu\bar{\nu})$+jets background contributions leads to an insignificant improvement in the background determination [1].

Finally, a control sample enriched in $t\bar{t}$ events is constructed using the same selection criteria as in the case of the $W(\to \mu\nu)$+jets but imposing that at least one of the jets is b-tagged.

6.2 Multijet background

The multijet background with large $E_{\mathrm{T}}^{\mathrm{miss}}$ mainly originates from the misreconstruction of the energy of a jet in the calorimeter and to a lesser extent is due to the presence of neutrinos in the final state from heavy-flavour hadron decays. In this analysis, the multijet background is determined from data, using the jet smearing method as described in Ref. [78], which relies on the assumption that the $E_{\mathrm{T}}^{\mathrm{miss}}$ of multijet events is dominated by fluctuations in the jet response in the detector which can be measured in the data. For the IM1 and EM1 selections, the multijet background constitutes about 0.3% and 0.4% of the total background, respectively, and it is negligible for the other signal regions.

6.3 Non-collision background

Remaining non-collision background contributions in the signal regions, mostly coming from muons originating in the particle cascades due to beam-halo protons intercepting the LHC collimators, are estimated following closely the methods set out in Ref. [77]. In particular, the jet timing, calculated from the energy-weighted average of the time of the jet energy deposits, defined with respect to the event time in nominal collisions, is used. A dedicated beam-induced background-enhanced region, defined by inverting the tight jet quality selection imposed on the leading jet, is used to estimate the amount of non-collision background from the fraction of events with a leading-jet absolute timing above 5 ns. The results indicate an almost negligible contribution from non-collision backgrounds in the signal regions.

6.4 Background fit

The use of control regions to constrain the normalization of the dominant background contributions reduces the relatively large theoretical and experimental systematic uncertainties, of the order of 20%–40%, associated with purely simulation-based background predictions in the signal regions. A complete study of systematic uncertainties is carried out, as detailed in Section 7. To determine the final uncertainty in the total background, all systematic uncertainties are treated as Gaussian-distributed nuisance parameters in a fit based on the profile likelihood method [79], which takes into account correlations among systematic variations. The likelihood also takes into account cross-contamination between different background sources in the control regions.

The $E_{\mathrm{T}}^{\mathrm{miss}}$ distribution is the observable used. A simultaneous background-only likelihood fit to the $E_{\mathrm{T}}^{\mathrm{miss}}$ distribution in the $W(\to \mu\nu)$+jets, $W(\to e\nu)$+jets, $Z/\gamma^{*}(\to \mu^{+}\mu^{-})$+jets, and top control regions is performed to normalize and constrain the background estimates in the signal regions. In the analysis, two different fitting strategies are considered, potentially giving slightly different results. A binned likelihood fit is performed using simultaneously all the exclusive $E_{\mathrm{T}}^{\mathrm{miss}}$ regions EM1–EM10, as described in Section 5. The fit includes a single floating normalization factor common for all W+jets and Z+jets processes, and a single floating normalization factor for top-quark related processes. The nuisance parameters, implementing the impact of systematic uncertainties, are defined bin-by-bin and correlations across $E_{\mathrm{T}}^{\mathrm{miss}}$ bins are properly taken into account. As a result, the fit exploits the information of the shape of the $E_{\mathrm{T}}^{\mathrm{miss}}$

distribution in constraining the normalization of W/Z+jets and top-quark related background. In addition, one-bin likelihood fits are performed separately for each of the inclusive regions IM1–IM10. In this case, the two normalization factors for W/Z+jets and top-quark related processes, respectively, and the nuisance parameters related to systematic uncertainties refer to the given $E_{\mathrm{T}}^{\mathrm{miss}}$ inclusive region.

The results of the background-only fit in the control regions are presented in Table 2 for the $E_{\mathrm{T}}^{\mathrm{miss}} >$ 250 GeV inclusive selection. As the table indicates, the W/Z+jets background predictions receive a multiplicative normalization factor of 1.27. Similarly, top-quark related processes receive a normalization factor of 1.06. When the binned-likelihood fit is performed simultaneously over the different exclusive $E_{\mathrm{T}}^{\mathrm{miss}}$ regions, thus including information from the shape of the measured $E_{\mathrm{T}}^{\mathrm{miss}}$ distribution, the normalization factor of the W/Z+jets background predictions remains essentially unchanged, dominated by the low-$E_{\mathrm{T}}^{\mathrm{miss}}$ region, and that of the top-quark related processes becomes 1.31.

Table 2: Data and background predictions in the control regions before and after the fit is performed for the $E_{\mathrm{T}}^{\mathrm{miss}} >$ 250 GeV inclusive selection. The background predictions include both the statistical and systematic uncertainties. The individual uncertainties are correlated, and do not necessarily add in quadrature to the total background uncertainty.

$E_{\mathrm{T}}^{\mathrm{miss}}$ **> 250 GeV Control Regions**	$W(\rightarrow \mu\nu)$	top	$W(\rightarrow e\nu)$	$Z/\gamma^*(\rightarrow \mu^+\mu^-)$
Observed events (36.1 fb^{-1})	110938	9729	68973	17372
SM prediction (post-fit)	110810 ± 350	9720 ± 130	69030 ± 260	17440 ± 130
$W(\rightarrow e\nu)$	7 ± 2	$0.17^{+0.44}_{-0.17}$	54500 ± 1000	0 ± 0
$W(\rightarrow \mu\nu)$	94940 ± 900	2160 ± 650	$7.20^{+7.49}_{-7.20}$	32 ± 3
$W(\rightarrow \tau\nu)$	5860 ± 160	164 ± 40	4110 ± 140	3 ± 1
$Z/\gamma^*(\rightarrow e^+e^-)$	0 ± 0	0 ± 0	5 ± 4	0 ± 0
$Z/\gamma^*(\rightarrow \mu^+\mu^-)$	1774 ± 75	59 ± 12	0.4 ± 0.2	16360 ± 160
$Z/\gamma^*(\rightarrow \tau^+\tau^-)$	277 ± 21	12 ± 2	212 ± 15	16 ± 3
$Z(\rightarrow \nu\bar{\nu})$	37 ± 3	6 ± 1	1.8 ± 0.3	0 ± 0
$t\bar{t}$, single top	4700 ± 790	7220 ± 820	8200 ± 1000	486 ± 64
Diboson	3220 ± 230	108 ± 38	2020 ± 160	540 ± 39
SM prediction from simulation (pre-fit)	87500 ± 8700	9200 ± 2000	56600 ± 5600	14100 ± 1400
$W(\rightarrow e\nu)$	5 ± 1	$0.15^{+0.41}_{-0.15}$	43300 ± 4700	0 ± 0
$W(\rightarrow \mu\nu)$	73700 ± 7900	1960 ± 580	$4.50^{+4.86}_{-4.50}$	24 ± 3
$W(\rightarrow \tau\nu)$	4600 ± 480	148 ± 37	3260 ± 350	2.2 ± 0.5
$Z/\gamma^*(\rightarrow e^+e^-)$	0 ± 0	0 ± 0	6 ± 5	0 ± 0
$Z/\gamma^*(\rightarrow \mu^+\mu^-)$	1420 ± 160	53 ± 11	0.5 ± 0.2	13100 ± 1400
$Z/\gamma^*(\rightarrow \tau^+\tau^-)$	226 ± 29	10 ± 2	175 ± 20	13 ± 3
$Z(\rightarrow \nu\bar{\nu})$	30 ± 4	5 ± 1	1.5 ± 0.3	0 ± 0
$t\bar{t}$, single top	4300 ± 1200	6900 ± 1800	7800 ± 2100	460 ± 120
Diboson	3180 ± 230	128 ± 44	2050 ± 170	541 ± 40

Figures 2 and 3 show the distributions of the $E_{\mathrm{T}}^{\mathrm{miss}}$ and the leading-jet p_{T} in data and MC simulation in the different control regions. In this case, the MC predictions include the data-driven normalization factors as extracted from the binned-likelihood fit to the different exclusive $E_{\mathrm{T}}^{\mathrm{miss}}$ bins. Altogether, the MC simulation provides a good description of the shape of the measured distributions in the different control regions.

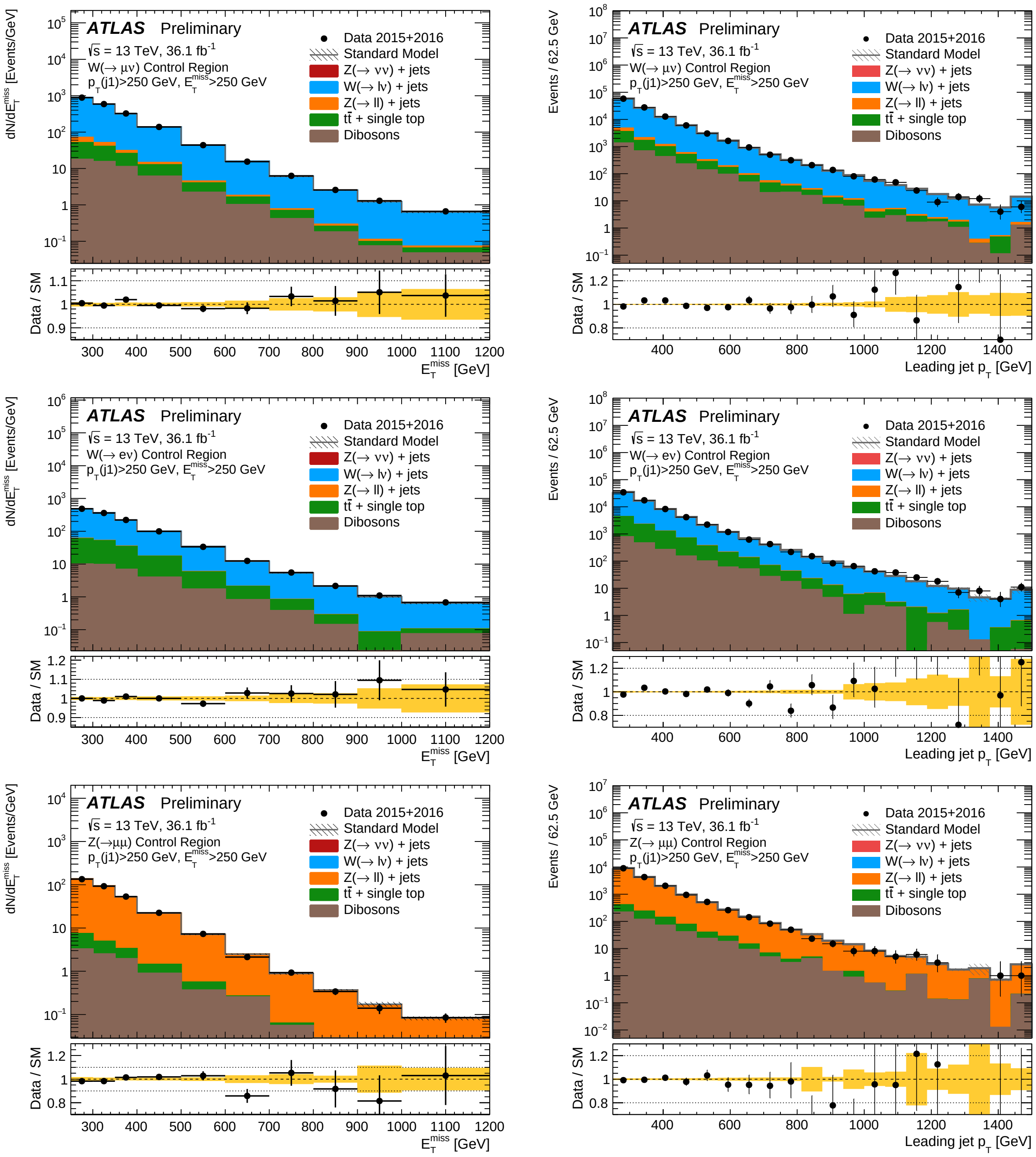

Figure 2: The measured $E_{\mathrm{T}}^{\mathrm{miss}}$ (left) and leading-jet p_{T} (right) distributions in the $W(\rightarrow \mu\nu)$+jets (top), $W(\rightarrow e\nu)$+jets (middle), and $Z/\gamma^{*}(\rightarrow \mu^{+}\mu^{-})$+jets (bottom) control regions, for the $E_{\mathrm{T}}^{\mathrm{miss}} > 250$ GeV inclusive selection, compared to the background predictions. The latter include the global normalization factors extracted from the fit. The error bands in the ratios include the statistical and experimental uncertainties in the background predictions as determined by the binned-likelihood fit to the data in the control regions. Where appropriate, the last bin of the distribution contains overflows. The contributions from multijet and non-collision backgrounds are negligible and are not shown in the figures.

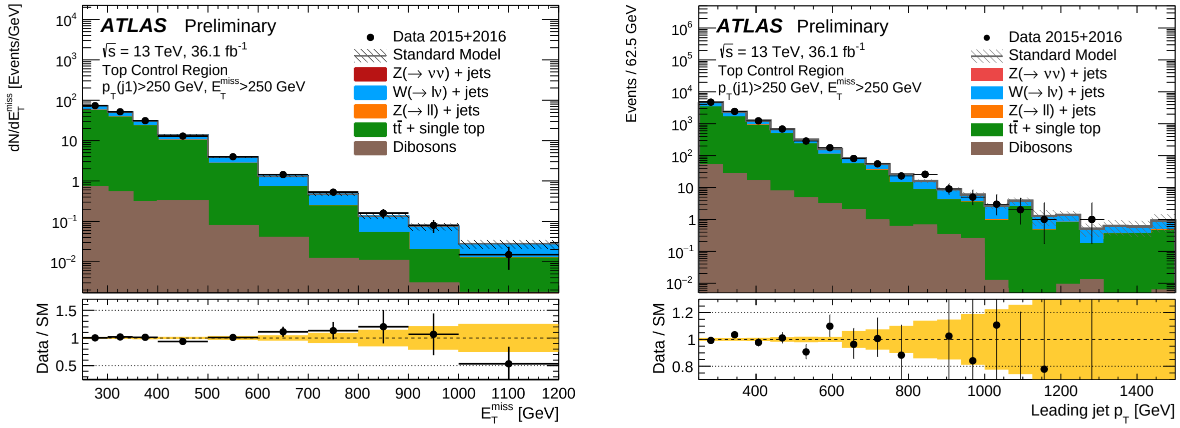

Figure 3: The measured $E_{\mathrm{T}}^{\mathrm{miss}}$ (left) and leading-jet p_{T} (right) distributions in the top control region, for the $E_{\mathrm{T}}^{\mathrm{miss}} > 250$ GeV inclusive selection, compared to the background predictions. The latter include the global normalization factors extracted from the fit. The error bands in the ratios include the statistical and experimental uncertainties in the background predictions as determined by the binned-likelihood fit to the data in the control regions. Where appropriate, the last bin of the distribution contains overflows. The contributions from multijet and non-collision backgrounds are negligible and are not shown in the figures.

7 Systematic uncertainties

In this section, the systematic uncertainties for both the background and signal models are presented. The impacts of the various sources of systematic uncertainty on the total background predictions are determined by the likelihood fits described in Section 6.4. Inclusive and exclusive $E_{\mathrm{T}}^{\mathrm{miss}}$ selections are considered separately. For the latter, correlations of systematic uncertainties across $E_{\mathrm{T}}^{\mathrm{miss}}$ bins are taken into account. The impact of the different sources of uncertainty in representative inclusive $E_{\mathrm{T}}^{\mathrm{miss}}$ bins, as determined using one-bin likelihood fits, are presented below. Experimental and theoretical uncertainties on the signal model are also presented.

7.1 Background systematic uncertainties

Uncertainties in the absolute jet and $E_{\mathrm{T}}^{\mathrm{miss}}$ energy scales and resolutions [68] translate into uncertainties in the total background which vary between ±0.5% for IM1 and ±5.3% for IM10. Uncertainties related to jet quality requirements, pileup description and corrections to the jet p_{T} and $E_{\mathrm{T}}^{\mathrm{miss}}$ introduce a ±0.9% to ±1.8% uncertainty in the background predictions. Uncertainties on the b-tagging efficiency, relevant for the definition of the $W(\rightarrow \mu\nu)$+jets and $t\bar{t}$ control regions, translate into an uncertainty in the total background that varies between ±0.9% for IM1 and ±0.5% for IM10. Uncertainties on soft contributions to $E_{\mathrm{T}}^{\mathrm{miss}}$ translate into an uncertainty on the total background yields that varies between ±0.4% for IM1 and ±1.7% for IM10.

Uncertainties in the simulated lepton identification and reconstruction efficiencies, energy/momentum scale and resolution translate into an uncertainty in the total background which vary between ±0.2% and ±1.7% for IM1 and between ±0.3 and ±2.3 for the IM10 selection, respectively.

Uncertainties on W/Z+jets predictions related to the modeling of parton-showers in Sherpa and the choice of PDFs translate into an uncertainty in the total background that varies between ±0.8% for IM1 and ±0.7% for IM10. Uncertainties on the implementation of higher-order QCD and electroweak parton-level calculations in the MC predictions, as described in Ref. [62], include: uncertainties on the QCD renomalization/factorization scales, affecting both the normalization and the shape of the predicted boson-p_{T} distribution; uncertainties on the non-universality of QCD corrections across W+jets and Z+jets processes; uncertainties on electroweak corrections beyond NNLO, unknown electroweak NLO correction terms at very high boson-p_{T}, and limitations of the Sudakov approximation adopted in the calculation; uncertainties on the QCD and electroweak interference terms; and uncertainties on the implementation of the higher-order QCD corrections in Sherpa, affected by a limited MC statistics at large boson-p_{T}. Altogether, this translates into an uncertainty on the total background that varies between ±0.4% for IM1 and ±2% for IM10.

Theoretical uncertainties in the predicted background yields for top-quark-related processes include variations in parton-shower parameters and the amount of initial- and final-state soft gluon radiation, and the difference between predictions from different MC generators. This introduces an uncertainty in the total background of about ±0.3% for the IM1, becoming negligible at very high $E_{\mathrm{T}}^{\mathrm{miss}}$.

Uncertainties in the diboson contribution are estimated by the difference in yields of the Sherpa and Powheg generators, after taking into account the difference in cross sections, which is then summed in quadrature with a ±6% theory uncertainty on the NLO cross section. This translates into an uncertainty on the total background of about ±0.2% for IM1 and about ±0.8% for IM10.

Uncertainties on the estimation of multijet and non-collision backgrounds translate into a ±0.5% uncertainty of the total background for IM1 and have a negligible impact on the total background predictions at larger $E_{\mathrm{T}}^{\mathrm{miss}}$. Similarly, the ±3.2% uncertainty in the integrated luminosity is included in the fit. It partially cancels in the data-driven determination of the SM background and translates into an uncertainty on the total background yield of about ±0.1% for IM1.

7.2 Signal systematic uncertainties

Sources of systematic uncertainty in the predicted signal yields are considered separately for each model of new physics using a common set of procedures. The procedures are described here, while the numerical uncertainties are given with the associated results for each model in Section 8. Experimental uncertainties include those related to the jet and $E_{\mathrm{T}}^{\mathrm{miss}}$ reconstruction, energy scales and resolutions, and the integrated luminosity. Other uncertainties related to the jet quality requirements are negligible.

Uncertainties affecting the signal acceptance in the generation of signal samples include: uncertainties on the modelling of the initial- and final-state gluon radiation, determined using simulated samples with modified parton-shower parameters (by factors of two or one half); uncertainties due to PDF and variations of the $\alpha_{\mathrm{s}}(m_Z)$ value employed, as computed from the envelope of CT10, MMHT2014 [80] and NNPDF30 error sets; and uncertainties due to the choice of renormalization and factorization scales. In addition, theoretical uncertainties in the predicted cross sections, including PDF and renormalization- and factorization-scale uncertainties, are computed separately for the different models.

8 Results and interpretation

The number of events in the data and the individual expected background predictions in several inclusive and exclusive signal regions, as determined using the background estimation procedure discussed in Section 6.4, are presented in detail in Tables 3 and 4. The results for all the signal regions are summarized in Table 5. Good agreement is observed between the data and the SM predictions in each case. The SM predictions for the inclusive selections are determined with a total uncertainty of ±2.4%, ±2.7%, and ±9.7% for the IM1, IM5, and IM10 signal regions, respectively, which include correlations between uncertainties in the individual background contributions.

Figure 4 shows several measured distributions compared to the SM predictions in the region $E_{\mathrm{T}}^{\mathrm{miss}} > 250$ GeV, for which the normalization factors applied to the MC predictions, and the related uncertainties, are determined from the global fit carried out in exclusive $E_{\mathrm{T}}^{\mathrm{miss}}$ bins. For illustration purposes, the distributions include the impact of different ADD, SUSY, and WIMP scenarios. In general, the SM predictions provide a good description of the measured distributions. The differences observed in the jet multiplicity distribution do not have an impact in the analysis. Statistical tests using the binned profile likelihood fit described above, and considering different scenarios for new physics, give p-values for a background-only hypothesis in the range 0.01–0.04, corresponding to a compatibility with the SM predictions within approximately 1.7σ to 2.1σ.

Table 3: Data and SM background predictions in the signal region for several inclusive $E_{\mathrm{T}}^{\mathrm{miss}}$ selections, as determined using separate one-bin likelihood fits in the control regions. For the SM prediction, both the statistical and systematic uncertainties are included. In each signal region, the individual uncertainties for the different background processes can be correlated, and do not necessarily add in quadrature to the total background uncertainty.

Inclusive Signal Region	IM1	IM3	IM5	IM7	IM10
Observed events (36.1 fb^{-1})	255486	76808	13680	2122	245
SM prediction	245900 ± 5800	73000 ± 1900	12720 ± 340	2017 ± 90	238 ± 23
$W(\rightarrow e\nu)$	20600 ± 620	4930 ± 220	682 ± 33	63 ± 8	7 ± 2
$W(\rightarrow \mu\nu)$	20860 ± 840	5380 ± 280	750 ± 44	115 ± 13	17 ± 2
$W(\rightarrow \tau\nu)$	50300 ± 1500	12280 ± 520	1880 ± 63	261 ± 13	24 ± 3
$Z/\gamma^{*}(\rightarrow e^{+}e^{-})$	0.11 ± 0.03	0.03 ± 0	0 ± 0	0 ± 0	0 ± 0
$Z/\gamma^{*}(\rightarrow \mu^{+}\mu^{-})$	564 ± 32	107 ± 9	10 ± 1	1.8 ± 0.5	0.2 ± 0.2
$Z/\gamma^{*}(\rightarrow \tau^{+}\tau^{-})$	812 ± 32	178 ± 8	24 ± 1	3.5 ± 0.5	0.4 ± 0.1
$Z(\rightarrow \nu\bar{\nu})$	137800 ± 3900	45700 ± 1300	8580 ± 260	1458 ± 76	176 ± 18
$t\bar{t}$, single top	8600 ± 1100	2110 ± 280	269 ± 42	26 ± 10	0 ± 1
Dibosons	5230 ± 400	2220 ± 170	507 ± 64	88 ± 19	13 ± 4
Multijet background	700 ± 700	51 ± 50	8 ± 8	1 ± 1	0.1 ± 0.1
Non-collision background	360 ± 360	51 ± 51	4 ± 4	0 ± 0	0 ± 0

The levels of agreement between the data and the SM predictions for the total number of events in inclusive and exclusive signal regions are translated into upper limits for the presence of new phenomena, using a simultaneous likelihood fit in both the control and signal regions, and the CL_s modified frequentist approach [81]. As already mentioned, the inclusive regions are used to set model-independent exclusion limits, and the exclusive regions are used for the interpretation of the results within different models for new physics. In general, the observed exclusion limits are worse than the expected sensitivity due to the slight excess of events in the data compared to the SM predictions, as shown in Table 5.

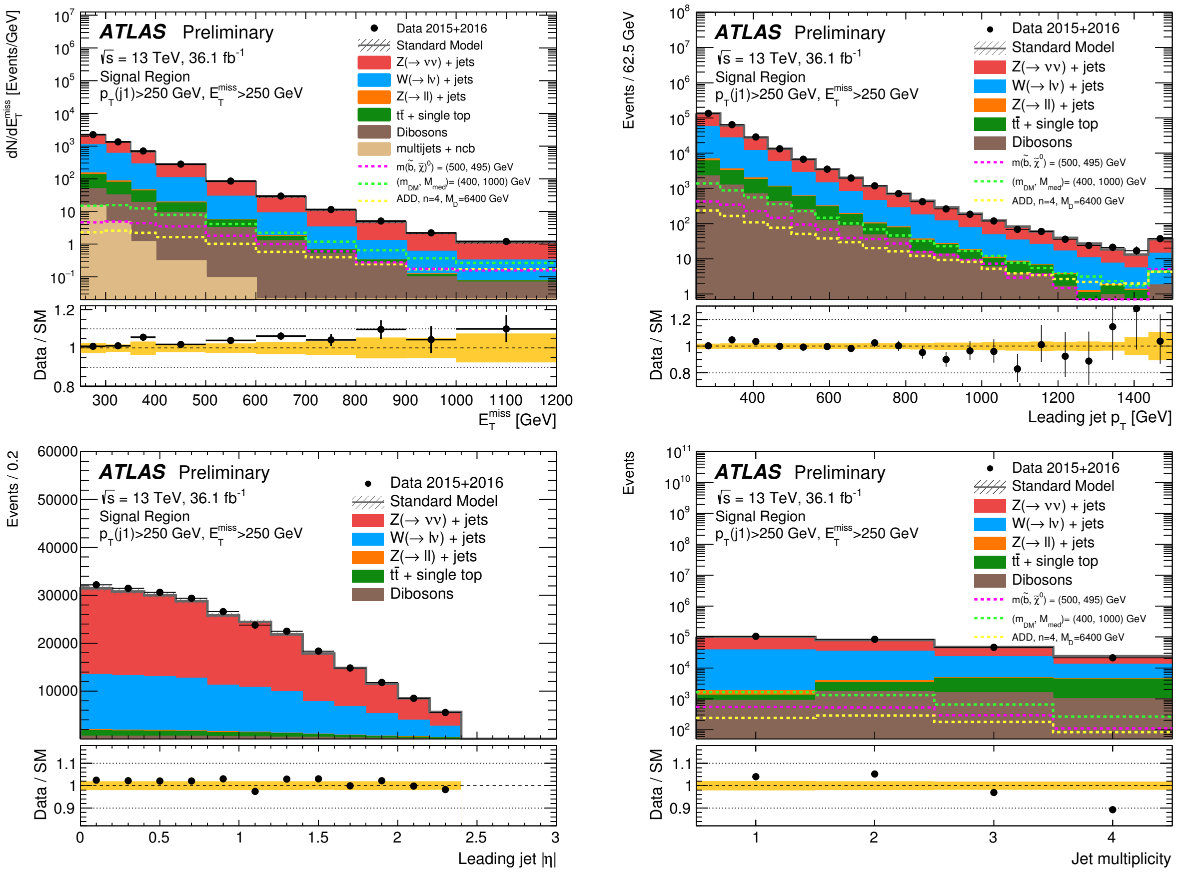

Figure 4: Measured distributions of the $E_{\mathrm{T}}^{\mathrm{miss}}$ (top-left), leading-jet p_{T} (top-right), leading-jet $|\eta|$ (bottom-left), and jet multiplicity (bottom-right) for the $E_{\mathrm{T}}^{\mathrm{miss}} > 250$ GeV selection compared to the SM predictions. The latter are normalized with normalization factors as determined by the global fit that considers exclusive $E_{\mathrm{T}}^{\mathrm{miss}}$ regions. For illustration purposes, the distributions of different ADD, SUSY, and WIMP scenarios are included. The error bands in the ratios shown in the lower panels include both the statistical and systematic uncertainties in the background predictions. Where appropriate, the last bin of the distribution contains overflows.

8.1 Model-independent exclusion limits

A likelihood fit is performed separately for each of the inclusive regions IM1–IM10. As a result, model-independent observed and expected 95% confidence level (CL) upper limits on the visible cross section, defined as the product of production cross section, acceptance and efficiency $\sigma \times A \times \epsilon$, are extracted, taking into consideration the systematic uncertainties in the SM backgrounds and the uncertainty in the integrated luminosity. The results are presented in Table 6. Values of $\sigma \times A \times \epsilon$ above 531 fb (for IM1) and above 1.6 fb (for IM10) are excluded at 95% CL.

8.2 Weakly-interacting massive particles

The results are translated into exclusion limits on the WIMP pair-production. Different simplified models are considered with either the exchange of an axial-vector or a pseudoscalar mediator in the *s*-channel.

Table 4: Data and SM background predictions in the signal region for several exclusive $E_{\mathrm{T}}^{\mathrm{miss}}$ selections, as determined using a binned likelihood fit in the control regions. For the SM prediction, both the statistical and systematic uncertainties are included. In each signal region, the individual uncertainties for the different background processes can be correlated, and do not necessarily add in quadrature to the total background uncertainty.

Exclusive Signal Region	EM2	EM4	EM6	EM8	EM9
Observed events (36.1 fb^{-1})	67475	27843	2975	512	223
SM prediction	67100 ± 1400	27640 ± 610	2825 ± 78	463 ± 19	213 ± 9
$W(\to e\nu)$	5510 ± 140	1789 ± 59	147 ± 9	18 ± 1	8 ± 1
$W(\to \mu\nu)$	6120 ± 200	2021 ± 82	173 ± 9	21 ± 5	11 ± 1
$W(\to \tau\nu)$	13680 ± 310	4900 ± 110	397 ± 11	55 ± 5	29 ± 2
$Z/\gamma^{*}(\to e^{+}e^{-})$	0.03 ± 0	0.02 ± 0.02	0 ± 0	0 ± 0	0 ± 0
$Z/\gamma^{*}(\to \mu^{+}\mu^{-})$	167 ± 8	36 ± 2	2 ± 0.2	0.4 ± 0.1	0.5 ± 0.1
$Z/\gamma^{*}(\to \tau^{+}\tau^{-})$	185 ± 6	68 ± 4	5.1 ± 0.3	0.3 ± 0.1	0.31 ± 0.04
$Z(\to \nu\bar{\nu})$	37600 ± 970	17070 ± 460	1933 ± 57	337 ± 12	153 ± 7
$t\bar{t}$, single top	2230 ± 200	848 ± 86	43 ± 6	4 ± 1	1.3 ± 0.4
Dibosons	1327 ± 90	874 ± 64	124 ± 16	26 ± 5	10 ± 2
Multijet background	170 ± 160	13 ± 13	1 ± 1	1 ± 1	0.1 ± 0.1
Non-collision background	71 ± 71	18 ± 18	0 ± 0	0 ± 0	0 ± 0

Table 5: Data and SM background predictions in the signal region for the different selections. For the SM predictions both the statistical and systematic uncertainties are included.

Inclusive Signal Region			**Exclusive Signal Region**		
Region	Predicted	Observed	Region	Predicted	Observed
IM1	245900 ± 5800	255486	EM1	111100 ± 2300	111203
IM2	138000 ± 3400	144283	EM2	67100 ± 1400	67475
IM3	73000 ± 1900	76808	EM3	33820 ± 940	35285
IM4	39900 ± 1000	41523	EM4	27640 ± 610	27843
IM5	12720 ± 340	13680	EM5	8360 ± 190	8583
IM6	4680 ± 160	5097	EM6	2825 ± 78	2975
IM7	2017 ± 90	2122	EM7	1094 ± 33	1142
IM8	908 ± 55	980	EM8	463 ± 19	512
IM9	464 ± 34	468	EM9	213 ± 9	223
IM10	238 ± 23	245	EM10	226 ± 16	245

In addition, the results obtained for an axial-vector mediator are then reinterpreted in terms of a vector mediator in the appendix.

In the case of the exchange of an axial-vector mediator, and for WIMP pair-production with $m_{Z_A} > 2m_{\chi}$, typical $A \times \epsilon$ values for the signal models with a 1 TeV mediator range from 25% to 0.4% for IM1 and IM10 selections, respectively.

The experimental uncertainties related to the jet and $E_{\mathrm{T}}^{\mathrm{miss}}$ scales and resolutions introduce uncertainties in the signal yields which vary between 2% and 7%. The uncertainty related to the modelling of the initial- and final-state radiation translates into ±20% uncertainty on the signal acceptance. The choice of different PDF sets results in up to ±20% uncertainty on the acceptance and ±10% uncertainty on the cross section. Varying the renormalization and factorization scales introduces ±5% variations of the cross section and a ±3% change in the acceptance. In addition, the uncertainty in the integrated luminosity is

Table 6: Observed and expected 95% CL upper limits on the number of signal events, S^{95}_{obs} and S^{95}_{exp}, and on the visible cross section, defined as the product of cross section, acceptance and efficiency, $\langle\sigma\rangle^{95}_{\mathrm{obs}}$, for the IM1–IM10 selections.

Signal channel	$\langle\sigma\rangle^{95}_{\mathrm{obs}}$ [fb]	S^{95}_{obs}	S^{95}_{exp}
IM1	531	19135	11700^{+4400}_{-3300}
IM2	330	11903	7000^{+2600}_{-2600}
IM3	188	6771	4000^{+1400}_{-1100}
IM4	93	3344	2100^{+770}_{-590}
IM5	43	1546	770^{+280}_{-220}
IM6	19	696	360^{+130}_{-100}
IM7	7.7	276	204^{+74}_{-57}
IM8	4.9	178	126^{+47}_{-35}
IM9	2.2	79	76^{+29}_{-21}
IM10	1.6	59	56^{+21}_{-16}

included.

A simultaneous fit to the signal and control regions in the exclusive $E_{\mathrm{T}}^{\mathrm{miss}}$ bins is performed, and used to set observed and expected 95% CL exclusion limits on the parameters of the model. Uncertainties in the signal acceptance times efficiency, the background predictions, and the luminosity are considered, and correlations between systematic uncertainties in signal and background predictions are taken into account. The fit accounts for the contamination of the control regions by signal events which a priori is estimated to be very small.

Figure 5 (left) shows the observed and expected 95% CL exclusion limits in the m_χ–m_{Z_A} parameter plane for a simplified model with an axial-vector mediator, Dirac WIMPs, and couplings $g_q = 1/4$ and $g_\chi = 1$. In addition, observed limits are shown using $\pm 1\sigma$ theoretical uncertainties in the signal cross sections. In the on-shell regime, the models with mediator masses up to 1.55 TeV are excluded for $m_\chi = 1$ GeV. This analysis loses sensitivity to the models in the off-shell regime, where cross-sections are suppressed due to the virtual production of the mediator. Perturbative unitarity is violated in the parameter region defined by $m_\chi > \sqrt{\pi/2}\, m_{Z_A}$ [82]. The masses corresponding to the relic density [83] as determined by the Planck and WMAP satellites [8, 9], within the WIMP dark matter model and in the absence of any interaction other than the one considered, are indicated in the figure as a line that crosses the excluded region at $m_{Z_A} \sim 1200$ GeV and $m_\chi \sim 440$ GeV. The region towards lower WIMP masses or higher mediator masses corresponds to dark-matter overproduction. On the opposite side of the curve, other mechanisms need to exist in order to explain the observed dark matter relic density.

The results are translated into 90% CL exclusion limits on the spin-dependent WIMP–proton scattering cross section σ_{SD} as a function of the WIMP mass, following the prescriptions explained in Refs. [12, 83]. Among results from different direct-detection experiments, in Figure 5 (right) the obtained exclusion limits in this analysis are compared to the most-stringent limits from the PICO direct-detection experiment [85]. This comparison is model-dependent and solely valid in the context of this particular Z'-like model. In this case, stringent limits on the scattering cross section of the order of 2.9×10^{-43} cm^2 (3.5×10^{-43} cm^2) for WIMP masses below 10 GeV (100 GeV) are inferred from this analysis, and com-

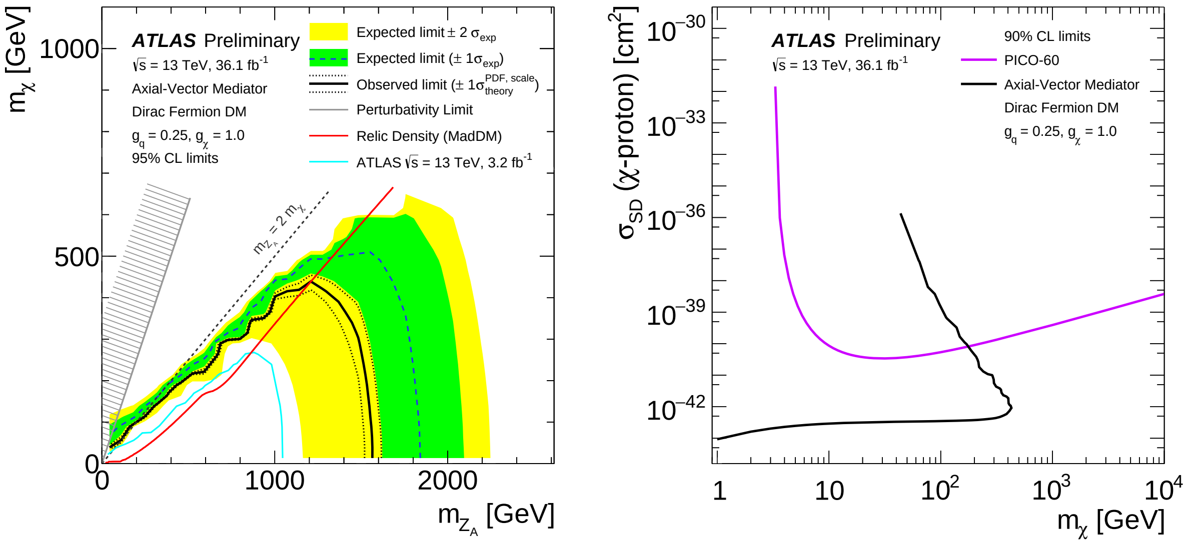

Figure 5: Left: 95% CL axial-vector exclusion contours in the m_χ–m_{Z_A} parameter plane. The solid (dashed) curve shows the median of the observed (expected) limit, while the bands indicate the $\pm 1\sigma$ theory uncertainties in the observed limit and $\pm 1\sigma$ and $\pm 2\sigma$ ranges of the expected limit in the absence of a signal. The red curve corresponds to the expected relic density, as computed with MadDM [84]. The region excluded due to perturbativity, defined by $m_\chi > \sqrt{\pi/2}\, m_{Z_A}$, is indicated by the hatched area. The dotted line indicates the kinematic limit for on-shell production $m_{Z_A} = 2 \times m_\chi$. The cyan line indicates previous results at 13 TeV [1] using 3.2 fb^{-1}. Right: A comparison of the inferred limits (black line) to the constraints from direct detection experiments (purple line) on the spin-dependent WIMP–proton scattering cross section in the context of the Z'-like simplified model with axial-vector couplings. Unlike in the m_χ–m_{Z_A} parameter plane, the limits are shown at 90% CL. The results from this analysis, excluding the region to the left of the contour, are compared with limits from the PICO [85] experiment. The comparison is model-dependent and solely valid in the context of this model, assuming minimal mediator width and the coupling values $g_q = 1/4$ and $g_\chi = 1$.

plement the results from direct-detection experiments for $m_\chi < 10$ GeV. The kinematic loss of model sensitivity is expressed by the turn of the WIMP exclusion line, reaching back to low WIMP masses and intercepting the exclusion lines from the direct-detection experiments at around $m_\chi = 200$ GeV.

A simplified model with a pseudo-scalar mediator (m_{Z_P}) was considered with couplings to quarks and dark matter equal to unity. As shown in Figure 6, for WIMP masses in the range 0–300 GeV and mediator masses m_{Z_P} in the range 0–700 GeV the analysis does not have yet enough sensitivity.

8.3 Squark pair production

Different models for squark pair production are considered: stop pair production with $\tilde{t}_1 \to c + \tilde{\chi}_1^0$, stop pair production with $\tilde{t}_1 \to b + ff' + \tilde{\chi}_1^0$, sbottom pair production with $\tilde{b}_1 \to b + \tilde{\chi}_1^0$, and squark pair production with $\tilde{q} \to q + \tilde{\chi}_1^0$ ($q = u, d, c, s$). In each case separately, the results are translated into exclusion limits as a function of the squark mass for different neutralino masses.

The results are translated into exclusion limits on the pair production of top squarks with $\tilde{t}_1 \to c + \tilde{\chi}_1^0$ (with branching fraction BR=100%) as a function of the stop mass for different neutralino masses. The typical $A \times \epsilon$ of the selection criteria varies, with increasing stop and neutralino masses, between 0.7%

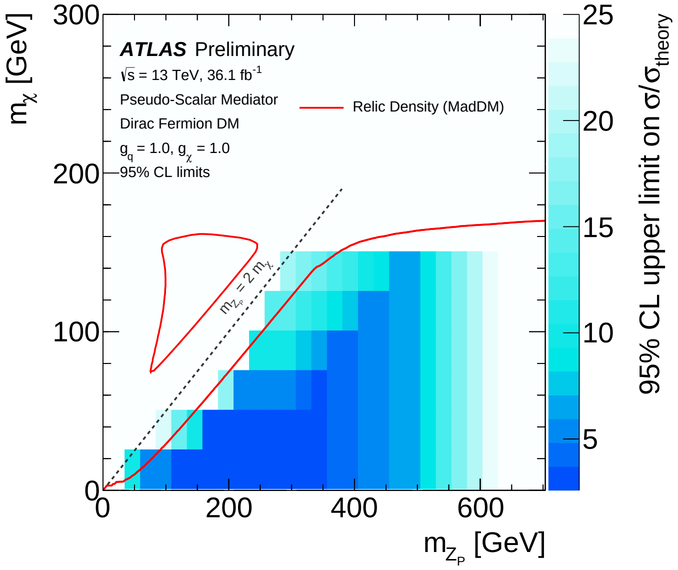

Figure 6: Observed 95% CL on the signal strength for the hypothesis of a pseudoscalar mediator, $g_q = g_\chi = 1.0$ and minimal mediator width, as a function of the assumed mediator and DM masses. The dotted line indicates the kinematic limit for on-shell production $m_{Z_P} = 2 \times m_\chi$. The part on the right of the continuous red line in the on-shell part of the plane (the closed area in the off-shell part) corresponds to predicted values of the relic density abundance inconsistent with the WMAP measurements (i.e. $\Omega h^2 > 0.12$), as computed with MadDM [84].

and 1.4% for IM1, and between 0.04% and 1.3% for IM10. Expected and observed 95% CL exclusion limits are set as in the case of the WIMP models. In addition, observed limits are computed using $\pm 1\sigma$ variations of the theoretical predictions for the SUSY cross sections.

The uncertainties related to the jet and $E_{\mathrm{T}}^{\mathrm{miss}}$ scales and resolutions introduce uncertainties in the signal yields which vary between ±1% and ±3% for different selections and squark and neutralino masses. In addition, the uncertainty in the integrated luminosity is included. The uncertainties related to the modelling of initial- and final-state gluon radiation translate into a ±7% to ±17% uncertainty in the signal yields. The uncertainties due to the PDFs result in a ±5% to ±17% uncertainty in the signal yields. Finally, the variations of the renormalization and factorization scales introduce a ±4% to ±13% uncertainty in the signal yields.

Figure 7 (left) presents the results in the case of the $\tilde{t}_1 \rightarrow c + \tilde{\chi}_1^0$ signal. The previous limits from the ATLAS Collaboration [1], corresponding to a luminosity of 3.2 fb^{-1}, are also shown. This analysis improves significantly the sensitivity at very low stop–neutralino mass difference. In the compressed scenario with the stop and neutralino nearly degenerate in mass, the exclusion extends up to stop masses of 430 GeV. The region with stop–neutralino mass difference below 5 GeV is not considered in the exclusion since in this regime the stop could become long-lived. Figure 7 (right) shows the expected and observed 95% CL exclusion limits as a function of the stop and neutralino masses for the $\tilde{t}_1 \rightarrow b + f f' + \tilde{\chi}_1^0$ (BR=100%) decay channel. For a $m_{\tilde{t}_1} - m_{\tilde{\chi}_1^0} \sim m_b$, stop masses up to 390 GeV are excluded at 95% CL.

Figure 8 (left) presents the expected and observed 95% CL exclusion limits as a function of the sbottom and neutralino masses for the $\tilde{b}_1 \rightarrow b + \tilde{\chi}_1^0$ (BR=100%) decay channel. In the scenario with $m_{\tilde{b}_1} - m_{\tilde{\chi}_1^0} \sim m_b$, this analysis extends the 95% CL exclusion limits up to a sbottom mass of 430 GeV. In the case of light neutralinos with $m_{\tilde{\chi}_1^0} \sim 1$ GeV, sbottom masses up to 610 GeV are excluded at 95% CL. Finally, Figure 8

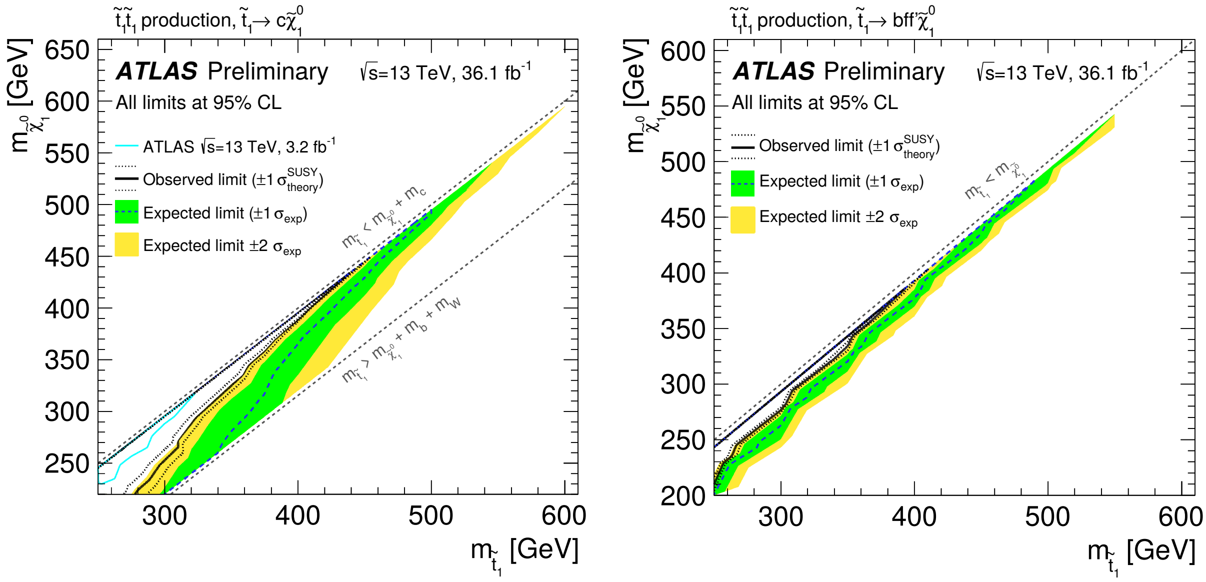

Figure 7: Excluded regions at the 95% CL in (left) the $(\tilde{t}_1, \tilde{\chi}_1^0)$ mass plane for the decay channel $\tilde{t}_1 \to c + \tilde{\chi}_1^0$ (BR = 100%) and (right) the decay channel $\tilde{t}_1 \to b + f f' + \tilde{\chi}_1^0$ (BR=100%). The dotted lines around the observed limits indicate the range of observed limits corresponding to $\pm 1\sigma$ variations on the NLO SUSY cross-section predictions. The bands around the expected limits indicate the expected $\pm 1\sigma$ and $\pm 2\sigma$ ranges of limits in the absence of a signal. The results from this analysis are compared to previous results from the ATLAS Collaboration at $\sqrt{s} = 13$ TeV [1] using 3.2 fb^{-1}.

(right) presents the observed and expected 95% CL exclusion limits as a function of the squark mass and the squark–neutralino mass difference for $\tilde{q} \to q + \tilde{\chi}_1^0$ $(q = u, d, c, s)$. In the compressed scenario with similar squark and neutralino masses, squark masses below 710 GeV are excluded at 95% CL. These results significantly extend previous exclusion limits [1].

8.4 Large extra spatial dimensions

The level of agreement between the data and the SM predictions is also translated into limits on the parameters of the ADD model. Only the signal regions with $E_{\mathrm{T}}^{\mathrm{miss}} > 400$ GeV, where the SM background is moderate and the shape difference between signal and the SM background becomes apparent, have an impact on the ADD limits. The typical $A \times \epsilon$ of the selection criteria varies, as the number of extra dimensions n increases from $n = 2$ to $n = 6$, between 13% and 17% for IM4 and between 0.8% and 1.4% for IM10.

The effect of experimental uncertainties related to jet and $E_{\mathrm{T}}^{\mathrm{miss}}$ scales and resolutions is found to be similar to the effect in the WIMP models. The uncertainties related to the modelling of the initial- and final-state gluon radiation translate into uncertainties in the ADD signal acceptance which vary between ±11% and ±13% with increasing $E_{\mathrm{T}}^{\mathrm{miss}}$ and approximately independent of n. The uncertainties due to the PDFs, affecting the predicted signal yields, increase from ±11% at $n = 2$ to ±43% at $n = 6$. Similarly, the variations of the renormalization and factorization scales introduce a ±23% to ±36% uncertainty in the signal yields, with increasing n.

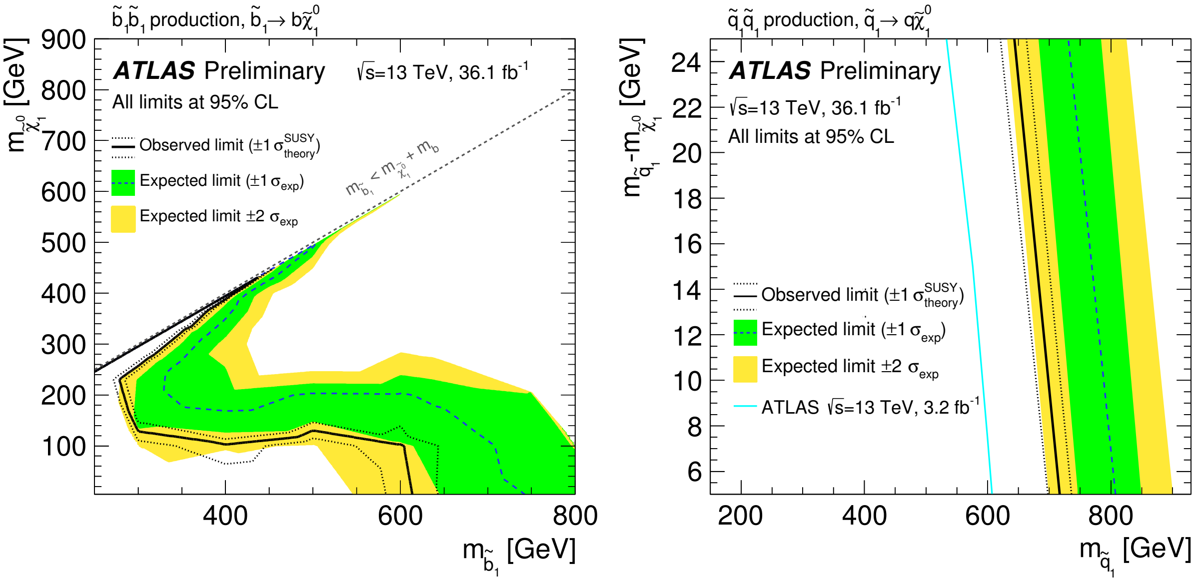

Figure 8: (left) Exclusion plane at 95% CL as a function of sbottom and neutralino masses for the decay channel $\tilde{b}_1 \rightarrow b + \tilde{\chi}_1^0$ (BR=100%). (right) Exclusion region at 95% CL as a function of squark mass and the squark–neutralino mass difference for $\tilde{q} \rightarrow q + \tilde{\chi}_1^0$ ($q = u, d, c, s$). The dotted lines around the observed limit indicate the range of observed limits corresponding to $\pm 1\sigma$ variations on the NLO SUSY cross-section predictions. The bands around the expected limit indicates the expected $\pm 1\sigma$ and $\pm 2\sigma$ ranges of limits in the absence of a signal. The results from this analysis are compared to previous results from the ATLAS Collaboration at $\sqrt{s} = 13$ TeV [1] using 3.2 fb^{-1}.

Expected and observed 95% CL exclusion limits are set as in the case of the WIMP and SUSY models. The -1σ variations of the ADD theoretical cross sections result in about a 7% to 10% decrease in the nominal observed limits, depending on n. Figure 9 and Table 7 present the results in the case of the ADD model. Values of M_D below 7.74 TeV at $n = 2$ and below 4.79 TeV at $n = 6$ are excluded at 95% CL, which extend the exclusion from previous results using 3.2 fb^{-1} of 13 TeV data [1].

As discussed in Refs. [13, 86], the analysis partially probes the phase-space region with $\hat{s} > M_D^2$, where $\sqrt{\hat{s}}$ is the centre-of-mass energy of the hard interaction. This challenges the validity of the model implementation and the lower bounds on M_D, as they depend on the unknown ultraviolet behavior of the effective theory. The observed 95% CL limits are recomputed after suppressing, with a weighting factor $M_D^4/\hat{s}^2$, the signal events with $\hat{s} > M_D^2$, here referred to as damping. This results in a negligible decrease of the quoted 95% CL lower limits on M_D, as also shown in Table 7.

Table 7: The 95% CL observed and expected lower limits on the fundamental Planck scale in $4 + n$ dimensions, M_D, as a function of the number of extra dimensions n, considering nominal LO signal cross sections. The impact of the $\pm 1\sigma$ theoretical uncertainty on the observed limits and the expected $\pm 1\sigma$ range of limits in the absence of a signal are also given. Finally, the 95% CL observed limits after damping of the signal cross section for $\hat{s} > M_D^2$ (see text) are quoted.

ADD Model Limits on $\mathbf{M_D}$ (95% CL)			
	Expected [TeV]	Observed [TeV]	Observed (damped) [TeV]
n = 2	$9.27^{+0.79}_{-0.96}$	$7.74^{+0.45}_{-0.55}$	7.74
n = 3	$7.12^{+0.48}_{-0.59}$	$6.22^{+0.36}_{-0.47}$	6.22
n = 4	$6.09^{+0.34}_{-0.43}$	$5.49^{+0.32}_{-0.45}$	5.49
n = 5	$5.54^{+0.27}_{-0.32}$	$5.11^{+0.30}_{-0.46}$	5.11
n = 6	$5.20^{+0.22}_{-0.26}$	$4.79^{+0.26}_{-0.47}$	4.77

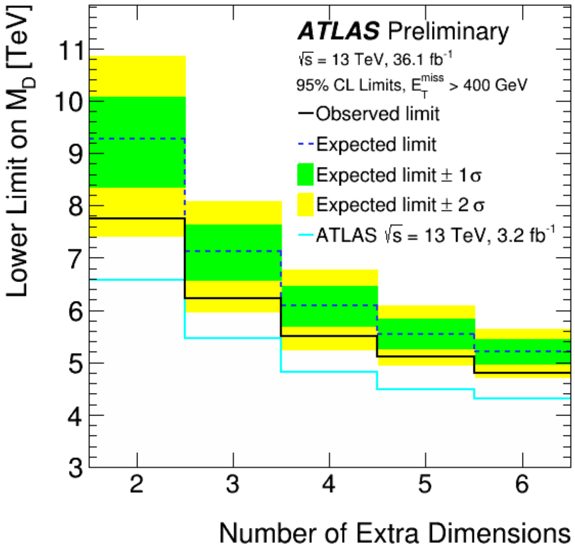

Figure 9: Observed and expected 95% CL lower limits on the fundamental Planck scale in $4 + n$ dimensions, M_D, as a function of the number of extra dimensions. The shaded area around the expected limit indicates the expected $\pm 1\sigma$ and $\pm 2\sigma$ range of limits in the absence of a signal. The 95% CL limits are computed with no suppression of the events with $\hat{s} > M_D^2$. The results from this analysis are compared to previous results from the ATLAS Collaboration at $\sqrt{s} = 13$ TeV [1] using 3.2fb^{-1}.

9 Conclusions

Results are reported from a search for new phenomena in events with an energetic jet and large missing transverse momentum in proton–proton collisions at $\sqrt{s} = 13$ TeV at the LHC, based on data corresponding to an integrated luminosity of 36.1 fb^{-1} collected by the ATLAS detector in 2015 and 2016. The measurements are in agreement with the SM predictions.

The results are translated into model-independent 95% confidence-level upper limits on $\sigma \times A \times \epsilon$ in the range 531–1.6 fb, decreasing with increasing missing transverse energy. The results are interpreted in terms of upper limits on the pair-production cross section of WIMPs. A simplified model is used with an axial-vector mediator and considering Dirac fermions as dark-matter candidates. Mediator masses below 1.55 TeV are excluded at 95% CL for very light WIMPs. These results are translated, in a model-dependent manner, into upper limits on spin-dependent contributions to the WIMP–nucleon elastic cross section as a function of the WIMP mass. WIMP–proton cross sections above 2.9×10^{-43} cm^2 (3.5×10^{-43} cm^2) are excluded at 90% CL for WIMP masses below 10 GeV (100 GeV), complementing results from direct-detection experiments.

Similarly, the results are interpreted in terms of the search for squark pair production in a compressed supersymmetric scenario. In the case of stop and sbottom pair production with $\tilde{t}_1 \rightarrow c + \tilde{\chi}_1^0$ or $\tilde{t}_1 \rightarrow b + ff' + \tilde{\chi}_1^0$ and $\tilde{b}_1 \rightarrow b + \tilde{\chi}_1^0$, respectively, squark masses below about 430 GeV are excluded at 95% CL. In the case of squark pair production with $\tilde{q} \rightarrow q + \tilde{\chi}_1^0$ ($q = u, d, c, s$), squark masses below 710 GeV are excluded. Altogether, these results extend the exclusion from previous ATLAS analyses.

Finally, the results are presented in terms of lower limits on the fundamental Planck scale M_D in $4 + n$ dimensions, versus the number of extra spatial dimensions in the ADD LED model. Values of M_D below 7.74 TeV at $n = 2$ and below 4.79 TeV at $n = 6$ are excluded at 95% CL.

References

[1] ATLAS Collaboration, *Search for new phenomena in final states with an energetic jet and large missing transverse momentum in pp collisions at $\sqrt{s} = 13$ TeV using the ATLAS detector*, Phys. Rev. **D94** (2016) 032005, arXiv: `1604.07773 [hep-ex]`.

[2] CMS Collaboration, *Search for dark matter produced with an energetic jet or a hadronically decaying W or Z boson at $\sqrt{s} = 13$ TeV* (2017), arXiv: `1703.01651 [hep-ex]`.

[3] V. Trimble, *Existence and Nature of Dark Matter in the Universe*, Ann. Rev. Astron. Astrophys. **25** (1987) 425–472.

[4] G. Bertone, D. Hooper and J. Silk, *Particle dark matter: Evidence, candidates and constraints*, Phys. Rept. **405** (2005) 279, arXiv: `hep-ph/0404175 [hep-ph]`.

[5] J. L. Feng, *Dark Matter Candidates from Particle Physics and Methods of Detection*, Ann. Rev. Astron. Astrophys. **48** (2010) 495–545, arXiv: `1003.0904 [astro-ph.CO]`.

[6] G. Steigman and M. S. Turner, *Cosmological Constraints on the Properties of Weakly Interacting Massive Particles*, Nucl. Phys. B **253** (1985) 375.

[7] E. W. Kolb and M. S. Turner, *The Early universe*, Front. Phys. **69** (1990) 1.

[8] Planck Collaboration, *Planck 2015 results. I. Overview of products and scientific results*, Astron. Astrophys. **594** (2016) A1, arXiv: `1502.01582 [astro-ph.CO]`.

[9] G. Hinshaw et al., *Nine-year Wilkinson Microwave Anisotropy Probe (WMAP) Observations: Cosmological Parameter Results*, ApJS **208**, 19 (Oct. 2013) 19, arXiv: `1212.5226`.

[10] J. Abdallah et al., *Simplified Models for Dark Matter Searches at the LHC*, Phys. Dark Univ. **9-10** (2015) 8, arXiv: `1506.03116 [hep-ph]`.

[11] D. Abercrombie et al., *Dark Matter Benchmark Models for Early LHC Run-2 Searches: Report of the ATLAS/CMS Dark Matter Forum* (2015), arXiv: `1507.00966 [hep-ex]`.

[12] O. Buchmueller et al., *Characterising dark matter searches at colliders and direct detection experiments: Vector mediators*, JHEP **01** (2015) 037, arXiv: `1407.8257 [hep-ph]`.

[13] ATLAS Collaboration, *Search for new phenomena in final states with an energetic jet and large missing transverse momentum in pp collisions at* $\sqrt{s}$ *=8 TeV with the ATLAS detector*, Eur. Phys. J. C **75** (2015) 299, [Erratum: Eur. Phys. J. C75 (2015) 408], arXiv: `1502.01518 [hep-ex]`.

[14] J. Goodman et al., *Constraints on Dark Matter from Colliders*, Phys. Rev. D **82** (2010) 116010, arXiv: `1008.1783 [hep-ph]`.

[15] G. Busoni et al., *On the Validity of the Effective Field Theory for Dark Matter Searches at the LHC*, Phys. Lett. B **728** (2014) 412, arXiv: `1307.2253 [hep-ph]`.

[16] H. Miyazawa, *Baryon Number Changing Currents*, Prog. Theor. Phys. **36 (6)** (1966) 1266.

[17] P. Ramond, *Dual Theory for Free Fermions*, Phys. Rev. D **3** (1971) 2415.

[18] Y. A. Golfand and E. P. Likhtman, *Extension of the Algebra of Poincare Group Generators and Violation of p Invariance*, JETP Lett. **13** (1971) 323.

[19] A. Neveu and J. H. Schwarz, *Factorizable dual model of pions*, Nucl. Phys. B **31** (1971) 86.

[20] A. Neveu and J. H. Schwarz, *Quark Model of Dual Pions*, Phys. Rev. D **4** (1971) 1109.

[21] J. Gervais and B. Sakita, *Field theory interpretation of supergauges in dual models*, Nucl. Phys. B **34** (1971) 632.

[22] D. V. Volkov and V. P. Akulov, *Is the Neutrino a Goldstone Particle?*, Phys. Lett. B **46** (1973) 109.

[23] J. Wess and B. Zumino, *A Lagrangian Model Invariant Under Supergauge Transformations*, Phys. Lett. B **49** (1974) 52.

[24] J. Wess and B. Zumino, *Supergauge Transformations in Four-Dimensions*, Nucl. Phys. B **70** (1974) 39.

[25] R. Barbieri and G. Giudice, *Upper Bounds on Supersymmetric Particle Masses*, Nucl. Phys. B **306** (1988) 63.

[26] P. Fayet, *Supersymmetry and Weak, Electromagnetic and Strong Interactions*, Phys. Lett. B **64** (1976) 159.

[27] P. Fayet, *Spontaneously Broken Supersymmetric Theories of Weak, Electromagnetic and Strong Interactions*, Phys. Lett. B **69** (1977) 489.

[28] G. R. Farrar and P. Fayet, *Phenomenology of the Production, Decay, and Detection of New Hadronic States Associated with Supersymmetry*, Phys. Lett. B **76** (1978) 575.

[29] P. Fayet, *Relations Between the Masses of the Superpartners of Leptons and Quarks, the Goldstino Couplings and the Neutral Currents*, Phys. Lett. B **84** (1979) 416.

[30] S. Dimopoulos and H. Georgi, *Softly Broken Supersymmetry and SU(5)*, Nucl. Phys. B **193** (1981) 150.

[31] N. Arkani-Hamed, S. Dimopoulos and G. Dvali, *The Hierarchy problem and new dimensions at a millimeter*, Phys. Lett. B **429** (1998) 263, arXiv: `hep-ph/9803315 [hep-ph]`.

[32] ATLAS Collaboration, *The ATLAS Experiment at the CERN Large Hadron Collider*, JINST **3** (2008) S08003.

[33] ATLAS Collaboration, *ATLAS Insertable B-Layer Technical Design Report*, CERN-LHCC-2010-013, 2010, URL: `http://cds.cern.ch/record/1291633`.

[34] ATLAS Collaboration, *2015 start-up trigger menu and initial performance assessment of the ATLAS trigger using Run-2 data*, ATL-DAQ-PUB-2016-001, 2016, URL: `http://cds.cern.ch/record/2136007`.

[35] ATLAS Collaboration, *The ATLAS Simulation Infrastructure*, Eur. Phys. J. C **70** (2010) 823, arXiv: `1005.4568 [physics.ins-det]`.

[36] S. Agostinelli et al., *GEANT4: A Simulation toolkit*, Nucl. Instrum. Meth. A **506** (2003) 250.

[37] T. Sjöstrand, S. Mrenna and P. Z. Skands, *PYTHIA 6.4 Physics and Manual*, JHEP **05** (2006) 026, arXiv: `hep-ph/0603175 [hep-ph]`.

[38] S. Alioli et al., *A general framework for implementing NLO calculations in shower Monte Carlo programs: the POWHEG BOX*, JHEP **06** (2010) 043, arXiv: `1002.2581 [hep-ph]`.

[39] S. Frixione, P. Nason and C. Oleari, *Matching NLO QCD computations with Parton Shower simulations: the POWHEG method*, JHEP **11** (2007) 070, arXiv: `0709.2092 [hep-ph]`.

[40] P. Nason, *A New method for combining NLO QCD with shower Monte Carlo algorithms*, JHEP **11** (2004) 040, arXiv: `hep-ph/0409146 [hep-ph]`.

[41] U. Haisch, F. Kahlhöfer and E. Re, *QCD effects in mono-jet searches for dark matter*, JHEP **12** (2013) 007, arXiv: `1310.4491 [hep-ph]`.

[42] U. Haisch and E. Re, *Simplified dark matter top-quark interactions at the LHC*, JHEP **06** (2015) 078, arXiv: `1503.00691 [hep-ph]`.

[43] R. D. Ball et al., *Parton distributions for the LHC Run II*, JHEP **04** (2015) 040, arXiv: `1410.8849 [hep-ph]`.

[44] ATLAS Collaboration, *ATLAS Run 1 Pythia8 tunes*, ATL-PHYS-PUB-2014-021, 2014, URL: `http://cds.cern.ch/record/1966419`.

[45] J. Alwall et al., *The automated computation of tree-level and next-to-leading order differential cross sections, and their matching to parton shower simulations*, JHEP **07** (2014) 079, arXiv: `1405.0301 [hep-ph]`.

[46] L. Lönnblad and S. Prestel, *Matching Tree-Level Matrix Elements with Interleaved Showers*, JHEP **03** (2012) 019, arXiv: `1109.4829 [hep-ph]`.

[47] W. Beenakker et al., *Stop production at hadron colliders*, Nucl. Phys. B **515** (1998) 3, eprint: `hep-ph/9710451`.

[48] W. Beenakker et al., *Supersymmetric top and bottom squark production at hadron colliders*, JHEP **08** (2010) 098, arXiv: `1006.4771 [hep-ph]`.

[49] W. Beenakker et al., *Squark and gluino hadroproduction*, Int. J. Mod. Phys. A **26** (2011) 2637, arXiv: `1105.1110 [hep-ph]`.

[50] C. Borschensky et al., *Squark and gluino production cross sections in pp collisions at $\sqrt{s}$ = 13, 14, 33 and 100 TeV*, Eur. Phys. J. C **74** (2014) 3174, arXiv: `1407.5066 [hep-ph]`.

[51] R. D. Ball et al., *Parton distributions with LHC data*, Nucl. Phys. B **867** (2013) 244, arXiv: `1207.1303 [hep-ph]`.

[52] T. Gleisberg et al., *Event generation with SHERPA 1.1*, JHEP **02** (2009) 007, arXiv: `0811.4622 [hep-ph]`.

[53] T. Gleisberg and S. Höche, *Comix, a new matrix element generator*, JHEP **12** (2008) 039, arXiv: `0808.3674 [hep-ph]`.

[54] F. Cascioli, P. Maierhofer and S. Pozzorini, *Scattering Amplitudes with Open Loops*, Phys. Rev. Lett. **108** (2012) 111601, arXiv: `1111.5206 [hep-ph]`.

[55] S. Schumann and F. Krauss, *A Parton shower algorithm based on Catani-Seymour dipole factorisation*, JHEP **03** (2008) 038, arXiv: `0709.1027 [hep-ph]`.

[56] S. Höche et al., *QCD matrix elements + parton showers: The NLO case*, JHEP **04** (2013) 027, arXiv: `1207.5030 [hep-ph]`.

[57] H.-L. Lai et al., *New parton distributions for collider physics*, Phys. Rev. D **82** (2010) 074024, arXiv: `1007.2241 [hep-ph]`.

[58] S. Catani et al., *Vector boson production at hadron colliders: a fully exclusive QCD calculation at NNLO*, Phys. Rev. Lett. **103** (2009) 082001, arXiv: `0903.2120 [hep-ph]`.

[59] S. Catani and M. Grazzini, *An NNLO subtraction formalism in hadron collisions and its application to Higgs boson production at the LHC*, Phys. Rev. Lett. **98** (2007) 222002, arXiv: `hep-ph/0703012 [hep-ph]`.

[60] A. D. Martin et al., *Parton distributions for the LHC*, Eur. Phys. J. **C63** (2009) 189–285, arXiv: `0901.0002 [hep-ph]`.

[61] J. M. Lindert et al., *Precise predictions for V+jets dark matter backgrounds* (2017), arXiv: `1705.04664 [hep-ph]`.

[62] ATLAS Collaboration, *Measurements of the production cross section of a Z boson in association with jets in pp collisions at $\sqrt{s}$ = 13 TeV with the ATLAS detector*, Eur. Phys. J. **C77** (2017) 361, arXiv: `1702.05725 [hep-ex]`.

[63] S. Frixione, P. Nason and G. Ridolfi, *A Positive-weight next-to-leading-order Monte Carlo for heavy flavour hadroproduction*, JHEP **09** (2007) 126, arXiv: `0707.3088 [hep-ph]`.

[64] D. J. Lange, *The EvtGen particle decay simulation package*, Nucl. Instrum. Meth. A **462** (2001) 152.

[65] M. Bahr et al., *Herwig++ Physics and Manual*, Eur. Phys. J. **C58** (2008) 639–707, arXiv: `0803.0883 [hep-ph]`.

[66] J. M. Campbell, R. K. Ellis and C. Williams, *Vector boson pair production at the LHC*, JHEP **07** (2011) 018, arXiv: `1105.0020 [hep-ph]`.

[67] M. Cacciari, G. P. Salam and G. Soyez, *The anti-k_t jet clustering algorithm*, JHEP **04** (2008) 063, arXiv: `0802.1189 [hep-ph]`.

[68] ATLAS Collaboration, *Jet energy measurement with the ATLAS detector in proton-proton collisions at* $\sqrt{s} = 7$ *TeV*, Eur. Phys. J. C **73** (2013) 2304, arXiv: `1112.6426 [hep-ex]`.

[69] ATLAS Collaboration, *Tagging and suppression of pileup jets with the ATLAS detector*, ATLAS-CONF-2014-018, 2014, URL: `http://cds.cern.ch/record/1700870`.

[70] ATLAS Collaboration, *Performance of b-Jet Identification in the ATLAS Experiment*, JINST **11** (2016) P04008, arXiv: `1512.01094 [hep-ex]`.

[71] ATLAS Collaboration, *Optimisation of the ATLAS b-tagging performance for the 2016 LHC Run*, ATL-PHYS-PUB-2016-012, 2016, URL: `https://cds.cern.ch/record/2160731`.

[72] ATLAS Collaboration, *Electron efficiency measurements with the ATLAS detector using the 2012 LHC proton–proton collision data*, ATLAS-CONF-2014-032, 2014, URL: `http://cdsweb.cern.ch/record/1706245`.

[73] ATLAS Collaboration, *Muon reconstruction performance of the ATLAS detector in proton–proton collision data at* $\sqrt{s}$ *=13 TeV*, Eur. Phys. J. **C76** (2016) 292, arXiv: `1603.05598 [hep-ex]`.

[74] ATLAS Collaboration, *Expected performance of missing transverse momentum reconstruction for the ATLAS detector at* $\sqrt{s} = 13$ *TeV*, ATL-PHYS-PUB-2015-023, 2015, URL: `https://cds.cern.ch/record/2037700`.

[75] ATLAS Collaboration, *Luminosity determination in pp collisions at* $\sqrt{s} = 8$ *TeV using the ATLAS detector at the LHC*, Eur. Phys. J. **C76** (2016) 653, arXiv: `1608.03953 [hep-ex]`.

[76] ATLAS Collaboration, *Selection of jets produced in 13 TeV proton-proton collisions with the ATLAS detector*, ATLAS-CONF-2015-029, 2015, URL: `http://cds.cern.ch/record/2037702`.

[77] ATLAS Collaboration, *Characterisation and mitigation of beam-induced backgrounds observed in the ATLAS detector during the 2011 proton-proton run*, JINST **8** (2013) P07004, arXiv: `1303.0223 [hep-ex]`.

[78] ATLAS Collaboration, *Search for squarks and gluinos with the ATLAS detector in final states with jets and missing transverse momentum using 4.7* fb^{-1} *of* $\sqrt{s} = 7$ *TeV proton-proton collision data*, Phys. Rev. D **87** (2013) 012008, arXiv: `1208.0949 [hep-ex]`.

[79] G. Cowan et al., *Asymptotic formulae for likelihood-based tests of new physics*, Eur. Phys. J. **C71** (2011) 1554, [Erratum: Eur. Phys. J. C73 (2013) 2501], arXiv: `1007.1727 [physics.data-an]`.

[80] L. A. Harland-Lang et al., *Parton distributions in the LHC era: MMHT 2014 PDFs*, Eur. Phys. J. C **75** (2015) 204, arXiv: `1412.3989 [hep-ph]`.

[81] A. L. Read, *Presentation of search results: The* CL_s *technique*, J. Phys. G **28** (2002) 2693–2704.

[82] F. Kahlhöfer et al.,
Implications of unitarity and gauge invariance for simplified dark matter models,
JHEP **02** (2016) 016, arXiv: `1510.02110 [hep-ph]`.

[83] G. Busoni et al., *Recommendations on presenting LHC searches for missing transverse energy signals using simplified s-channel models of dark matter* (2016), ed. by A. Boveia et al., arXiv: `1603.04156 [hep-ex]`.

[84] M. Backović et al., *Direct Detection of Dark Matter with MadDM v.2.0*,
Phys. Dark Univ. **9-10** (2015) 37–50, arXiv: `1505.04190 [hep-ph]`.

[85] C. Amole et al., *Dark Matter Search Results from the PICO-60 C_3F_8 Bubble Chamber*,
Phys. Rev. Lett. **118** (2017) 251301, arXiv: `1702.07666 [astro-ph.CO]`.

[86] ATLAS Collaboration, *Search for dark matter candidates and large extra dimensions in events with a jet and missing transverse momentum with the ATLAS detector*, JHEP **04** (2013) 075, arXiv: `1210.4491 [hep-ex]`.

Appendix

In Figure 10, the results are translated into 95% CL exclusion limits in the m_χ–m_{Z_V} parameter plane for a simplified model with a vector mediator, Dirac WIMPs, and couplings $g_q = 1/4$ and $g_\chi = 1$. The results are obtained from those for the axial-vector model, taking into account the cross section differences between models, motivated by the fact both models present compatible particle-level selection acceptances. For very light WIMPs, mediator masses below about 1.55 TeV are excluded.

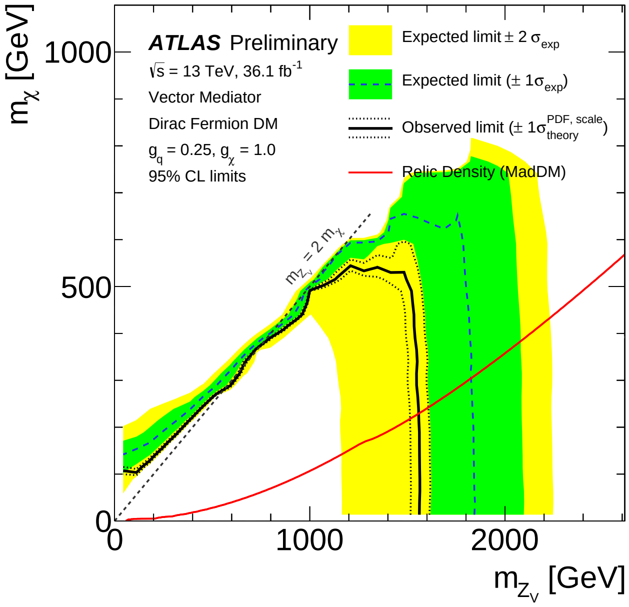

Figure 10: Observed (solid line) and expected (dashed line) exclusions at 95% CL on the vector mediator models with $g_q = 0.25, g_\chi = 1.0$ and minimal mediator width, as a function of the assumed mediator and DM masses. The regions within the drawn contours are excluded. The part on the right of the continuous red line corresponds to predicted values of the relic density abundance inconsistent with the WMAP measurements (i.e. $\Omega h^2 > 0.12$), as computed with MadDM [84]. The results are obtained from those for the axial-vector model, taking into account the cross section differences between models, motivated by the fact both models present compatible particle-level selection acceptances.